OLD DOMINION UNIVERSITY RESEARCH FOUNDATION

DEPARTMENT OF ELECTRICAL ENGINEERING
SCHOOL OF ENGINEERING
OLD DOMINION UNIVERSITY
NORFOLK, VIRGINIA

AN INVESTIGATION TO MODEL RADAR BACKSCATTER FROM RIDGED FIRST YEAR SEA ICE

By

Betty Lou W. Jackson

and

John W. Stoughton, Principal Investigator

Final Report
For the period ending December 31, 1981

Prepared for the
National Aeronautics and Space Administration
Langley Research Center
Hampton, Virginia

Under
Research Grant NAS1-15648
Task Authorization No. 51
William L. Grantham, Technical Monitor

August 1983

DEPARTMENT OF ELECTRICAL ENGINEERING
SCHOOL OF ENGINEERING
OLD DOMINION UNIVERSITY
NORFOLK, VIRGINIA

AN INVESTIGATION TO MODEL RADAR BACKSCATTER FROM RIDGED FIRST YEAR SEA ICE

By

Betty Lou W. Jackson

and

John W. Stoughton, Principal Investigator

Final Report
For the period ending December 31, 1981

Prepared for the
National Aeronautics and Space Administration
Langley Research Center
Hampton, Virginia

Under
Research Grant NAS1-15648
Task Authorization No. 51
William L. Grantham, Technical Monitor

Submitted by the
Old Dominion University Research Foundation
P.O. Box 6369
Norfolk, Virginia 23508

August 1983

TABLE OF CONTENTS

PAGE

LIST OF TABLES

LIST OF FIGURES

Symbol Definitions

B	the 3dB beamwidth of the RADSCAT antenna
b_r, b_f	intercepts of the linear approximations of the signature curves for rough and flat ice respectively
d	distance between laser samples
h(i)	height as measured by the laser profiler
i	index of facets in the equivalent resolution cell, 100 Hz
j	index of RADSCAT integrated resolution cells, 10 Hz
k	index of angle bins
m_r, m_f	slopes of the linear approximations of the signature curves for rough and flat ice respectively
$p(k)$	percentage of the facets of the equivalent resolution cell in the k^{th} bin
$p_{R/S}$	measured total return power in milliwatts, from the RADSCAT
p_{sim}	simulated total return power in milliwatts, the output of the model
$W(\theta)$	reflected power from surface due to antenna pattern and integration time
w(i)	dicrete weighting sequence used to approximate $W(\theta)$
$\alpha(i)$	surface slope of the i^{th} facet
$\phi(i)$	true incidence angle of the i^{th} facet, measured from the incident wave to the surface normal
ϕ_k	the average angle of the k^{th} angle bin
σ^o	normalized radar cross section, from Onstott's curves
$\sigma[\phi]$	strength of return, proportional to σ^o, used to calculate p_{sim}, in milliwatts
$\sigma_{dB}[\phi]$	$10 \log_{10} \sigma[\phi]$
$\sigma(\phi_k)$	average strength of return over the k^{th} range of angles
θ	angle measured from boresight of antenna
θ_n	the elevation angle of the antenna measured from nadir

AN INVESTIGATION TO MODEL RADAR BACKSCATTER FROM RIDGED FIRST YEAR SEA ICE

By

Betty Lou W. Jackson[1] and John W. Stoughton[2]

SUMMARY

This paper investigates the response of a radar type sensor, the microwave scatterometer, to meter scale roughness of first-year sea ice. The scatterometer measures the absolute backscattered power from target, and use of the radar equation permits calculation of the surface reflectivity expressed as the radar scattering coefficient, σ°, also called the normalized radar cross section. This project develops an empirical, one-dimensional model to predict the back-scattered power from ridged first-year sea ice of known surface topography, by interpreting the surface as a series of angular facets and summing the proportional power from each facet. The model is evaluated by comparing the predicted values to scatterometer measurements obtained during the National Aeronautics and Space Administration's (NASA's) Sea Ice Radar Experiment (SIRE) in 1978 and 1979.

The input to the model is surface slope, which for SIRE was calculated from the ice topography, as measured by an airborne laser profiler. By limiting our consideration to first-year ice, the modeled radar backscatter is a function of slope only. The correlation between the predicted and the measured power is .62-.68, and it is concluded that the model adequately describes the backscatter from regions of first year sea ice whose dimensions are of a few tens of meters.

---

[1] Graduate Research Assistant, Department of Electrical Engineering, School of Engineering, Old Dominion University, Norfolk, Virginia 23508.

[2] Associate Professor, Department of Electrical Engineering, School of Engineering, Old Dominion University, Norfolk, Virginia 23508.

CHAPTER ONE

INTRODUCTION

1.1 Background

Sea ice, the frozen surface of sea water, has a significant effect on our lives. At its maximum extent, this frozen layer covers $40.6 \times 10^{+6}$ km^2, nearly thirteen percent of the world's oceans. Sea ice plays a critical role in maintaining the earth's heat balance and directly influences the climate. It is an obstacle to shipping and to the recovery of an estimated 200 billion barrels of oil and 300 trillion cubic feet of natural gas [1]. Yet, despite its importance, less is known about sea ice than about any other part of the earth's surface. Only in this century have scientific ice expeditions reached the Arctic, and most of our present knowledge of sea ice has been acquired within the last two decades. To date, the properties of sea ice are not clearly described, much less understood.

1.2 Need for Ice Research

The study of sea ice has become interdisciplinary, from fore-

casting weather to mapping ocean currents and ice drift. Weeks [2] points out that meteorologists are interested in the patterns and locations of ice ridges and leads (open cracks in the ice sheet) because ridging and ice break-up become most severe in the period immediately preceding storms, and because ridges have a direct effect on the wind. Meteorologists suspect also that the location of the ice edge influences the frequency and paths of cyclones. Climatologists need data on surface temperatures, heat transfer and atmospheric pressure at high latitudes [3]. Oceanographers can study surface water currents by tracking ice floes. As reported by Weeks [4], they need information about the dispersion of dense melt water and about the effects of heat and salinity on ocean currents. Biologists are studying sea ice in an attempt to understand how the seasonal changes in ice temperature and salinity affect the life forms of the arctic area, and whether the ice biota affect the formation of the ice [4].

In addition to the scientific uses, there are commercial and industrial applications for ice information as well. Shipping could be speeded and its cost reduced if ice modelers could predict regions where leads will occur which would facilitate improved navigation within the ice zone. The design of ice breakers would be improved if the shipbuilding industry had realistic statistics for the average thickness and age of ice, and the number of ridges per nautical mile [5]. The petroleum industry requires accurate tactical ice forecasting since an unexpected ice movement or break-up could demolish offshore oil rigs [6], and grounded keels (underwater protrusions of

ridges) of land-fast ridges could easily scour the shore and seabottom causing extensive damage to cables and pipelines [7]. For defense purposes, the Navy has been studying the hydroacoustics of ice-covered water and the effects of ice keels on sonar [4]. Of late, there has been interest in icebergs as a source for fresh water for arid countries. It should be apparent that the need for ice research is real, and that it goes beyond simple scientific curiosity.

1.3 Need for Data About Ice Ridges

The characteristic of sea ice which is of concern in this thesis is ice ridging, which is loosely defined as a linear distribution (mound) of ice broken and buckled by compressive forces, and having heights of approximately 1/2 to several meters. As mentioned previously, the shipping and shipbuilding industries are significantly affected by ridges: their height, width, keel depth, location, orientation and distributions being the major ridge parameters of importance. The need exists for information on these parameters in real time and even future time (forecasting) for navigation, and over five to ten year timespans for ice breaker design.

Another application for ridge data is ice dynamics modeling. Ridges form where leads have previously occurred; as a result, by utilizing past years' data, modelers can test their predictions of where leads are likely to occur. Because the water in open leads permits greater heat transfer than the surrounding ice, the location of leads is an important input to climatology as well as to weather

forecasting. The wind is a factor in the direction and velocity of ice movement and is therefore a factor in ridge formation. The ridges, in turn, affect the wind drag of the ice, changing the force which produced them [2]. A better understanding of the effect ridges and leads have on the wind would enable meteorologists to make more accurate weather forecasts, and the input of ridge location to ice forecasters' models would allow better prediction of ice movement [8].

1.4 Measurement Techniques

Due to the inhospitable climate and the difficult access to the ice fields, the information available to researchers has been limited. Prior to the 1960's the ice data set consisted only of observations made from ships, sparse measurements made from surface based camps, and interpretations of aerial photograms (scaled photography). After considering some of the ice information required, such as surface temperatures, ice salinity and density, ice age and thickness, lead patterns, and ridge distributions, it becomes apparent that these three methods of collecting ice data are not capable of producing a synoptic view of the Arctic. Ships are restricted to the open water; otherwise they run the risk of being frozen into the ice mass. Reinforced vessels, which would be able to enter the ice field, are prohibitively expensive. Scientists working from surface based camps located farther into the ice pack can make extensive measurements from an area up to 10 km square. The surface data and ice cores they collect can provide valuable, but very localized,

information on ice structure. Through aerial reconnaissance wider areas can be covered, but since the Arctic is in constant thermal flux, the area is frequently cloud-covered and turbulent, which limits the opportunities for flight. The long periods of arctic darkness allow little aerial photogrammetry even when the weather permits. An ice monitoring system needs to be developed which can be used over the expanses of the Arctic which is functional during poor weather and darkness, and which is preferably not surface based. Studies are being conducted on an alternate technique which can meet all of these requirements; that technique is remote sensing by satellites.

Many remote sensors are under continued investigation to determine their feasibility for ice monitoring and are being developed for satellite application based largely on encouraging results from aircraft experiments. Weeks summarized the current state of remote sensing [9]. Imaging, visible sensors, such as the Very High Resolution Radiometer (VHRR) on board the National Oceanic and Atmospheric Administration's (NOAA's) satellites, and the multispectral scanning system flown on the Landsat satellite, have shown the capability to resolve large scale features (80 - 800 m) and thereby permit the tracking of ice floes and the icepack. Lower resolution thermal sensors, also on board the NOAA satellite, are being used to define large leads and ice extent by differentiating between the temperature of ice and the surrounding water. Whereas the optical and infrared remote sensors require clear skies (and suitable lighting for the visible), the use of passive microwave sensors allows

penetration of moderate cloud-cover as well as day and night operation to distinguish between ice and water as well as between ice types (ie., multi-year, first-year and thin ice). This technique uses sensitive microwave receivers (radiometers) to measure a gray-body electromagnetic radiation from ice and water which differ because of their emissivities and temperatures. Microwave radiometers have been deployed on Nimbus-5, 7 and 8 satellites. Among active microwave systems, there are studies on radar altimeters, synthetic aperture radar (SAR) and scatterometers. Radar altimeters, flown on Geos-3 and Seasat satellites, are nadir-looking radars which measure the height above the surface with a resolution of a few centimeters. For ice remote sensing, the altimeters use the difference in backscattering amplitude to distinguish the ice/water boundaries. SAR and scatterometry both measure the strength of the radar return to provide roughness information, whether the surface is ice or water. SAR employs digital co. ela:'on processing to synthesize the large antenna necessary to provide a good resolution image (approximately 25 km) from space. Ice parameter extraction algoritnms for SAR are based on photo-interpretation techniques. The scatterometer is a quantitative active microwave sensor and has the ability to discriminate between water and ice and between multi-year and first-year ice over coarser resolution of tens of kilometers from satellite altitudes. Both SAR and scatterometer were on-board Seasat.

Of these remote sensors, it is the data from the microwave scatterometer which will provide the comparison data set for the model

developed in this thesis. Further, the laser profiler and the mapping camera will be used as auxiliary sources of data to calculate the scatterometer response to ice roughness.

1.5 Research Objectives

Specifically, in this thesis, an empirical model is developed to predict the backscatter from ridged first-year sea ice, given the one-dimensional surface slope as the only input parameter. Experimental data are used where the slope is determined from the ice surface topography provided by the laser profiler, and comparisons are made between the calculated backscattered power and the value measured by the scatterometer to establish the validity of the model. The premise is, that if the above comparisons are highly correlated, then the model can be used to simulate the response of a satellite radar sensor, and thereby evaluate if the scatterometer can be used over first year sea ice to measure the degree of ridging. It is not within the scope of this thesis to reverse the modeling process and develop an algorithm to quantify the roughness based on scatterometer data.

To this author's knowledge, investigations such as this have not been made. Models have been developed using existing data to describe and predict the physical phenomena of ice, such as ridge height or drift direction [10,11]. Further, theorists have been attempting to develop electromagnetic models to predict the volume and surface scattering of sea ice [12,13]. However, we know of no work where the response of a radar sensor to ice ridges has been modeled.

The instruments used in this thesis are discussed in Chapter Two, along with the significant details of the Sea Ice Radar Experiment aircraft missions of 1978 and 1979 (SIRE). Data processing for the laser is also discussed in that chapter.

The modeling processes will be described in Chapter Three, and will include the development of the model. Results of the model simulation will be presented in Chapter Four. The predicted versus observed backscatter correlation will be determined, as well as the results of tests for statistical significance. Conclusions and future research implications will be given in Chapter Five.

CHAPTER TWO

INSTRUMENTATION AND DATA PROCESSING

2.1 Introduction

In response to the need for remote sensing of ice, as discussed in the introduction, the National Aeronautics and Space Administration (NASA) has conducted a number of microwave remote sensing experiments. This thesis uses data acquired on two aircraft missions, Sea Ice Radar Experiments (SIRE) in 1978 and 1979, designed specifically to investigate the effect of sea ice ridging on radar instruments. SIRE 1978 and SIRE 1979 occurred during the winter ice seasons of those years. Both missions were conducted in the Beaufort Sea off northern Alaska, and the data for this thesis were collected exclusively in the Prudhoe Bay region. Typical aircraft ground tracks are shown in Figure 2.1. These flight lines consisted of flying over heavily ridged ice at an altitude of 300 to 500 meters, for distances of approximately 25 km. During each flight line, data were obtained simultaneously from optical and radar sensors.

This chapter will discuss only those instruments used during SIRE which are of interest to our investigations; namely, the aerial

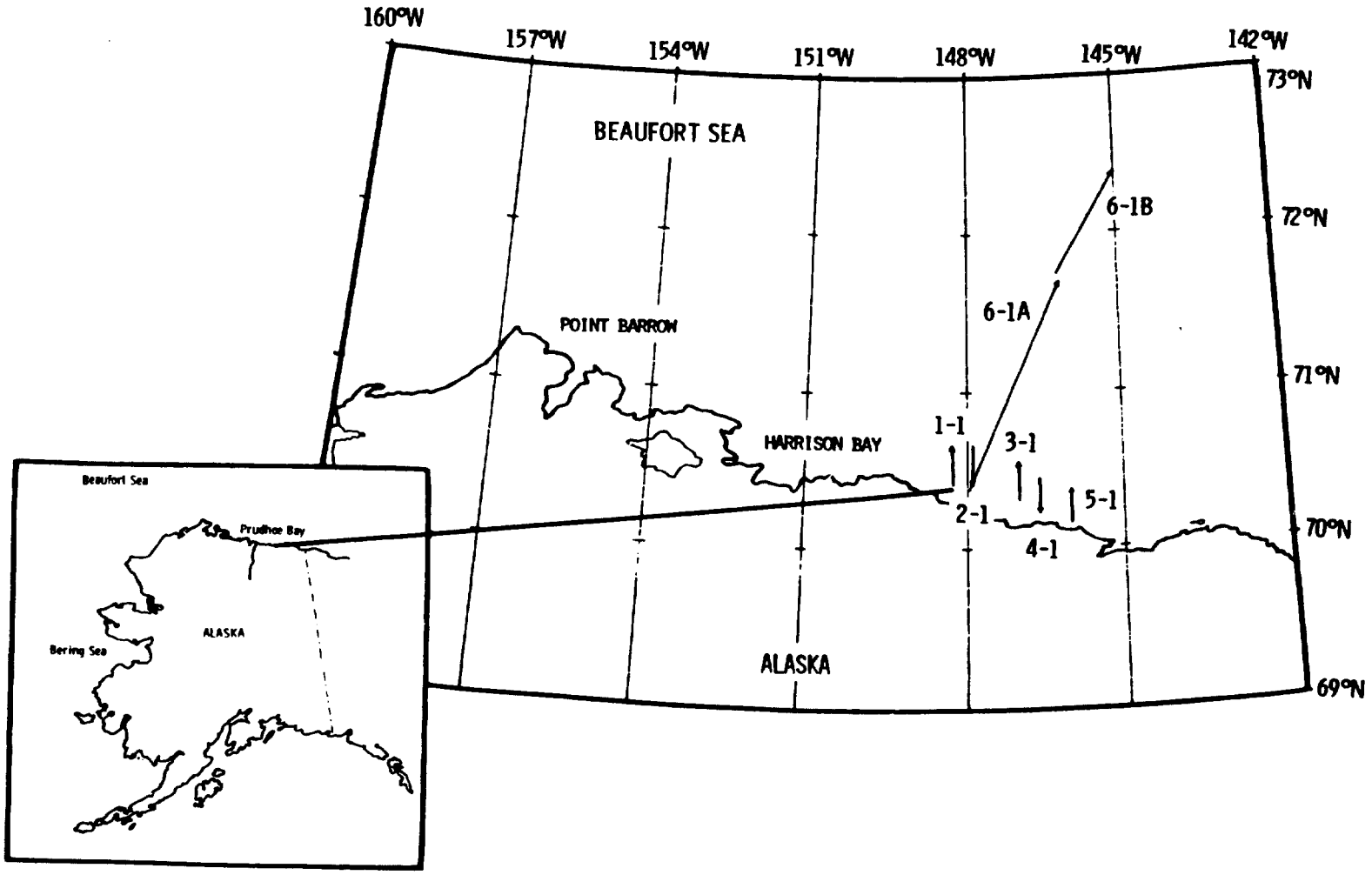

Figure 2.1. Flight Lines for SIRE 1979 for March 12, 1979

mapping camera, the laser profiler and the microwave scatterometer. The first two are used to establish the input data set to the radar backscatter model; whereas the data from the scatterometer are used for comparison and evaluation. Figure 2.2 illustrates the positions of the instruments on the airplane and the locations and relative sizes of their footprints (area of illumination on the surface). Also discussed in this chapter are the data processing methods used to prepare the input to the model. Examples are presented which indicate how the data was edited to constrain the ice surface parameters.

2.2 Mapping Camera

If one eliminates observations from ships, which are a form of "remote sensing," then aerial photogrammetry is the first remote sensing method used in sea ice study, and certainly the first to provide wide area coverage. Although use of the aerial mapping camera is limited to clear weather and daylight, the information available from this instrument is extremely helpful to ice investigators.

Through photogrammetric interpretation it is possible to calculate ridge height from shadows and to estimate age and thickness of the ice, provided that the snow cover has not obscured the surface texture and color tone. Figures 2.3 and 2.4 are facsimiles of typical aerial photograms. It is seen from these that the thinner the ice, the greyer it appears in the photogram, with water and extremely young ice appearing almost black. Multi-year ice (ice which has survived at least one melt season) is much thicker than first-year ice and can be

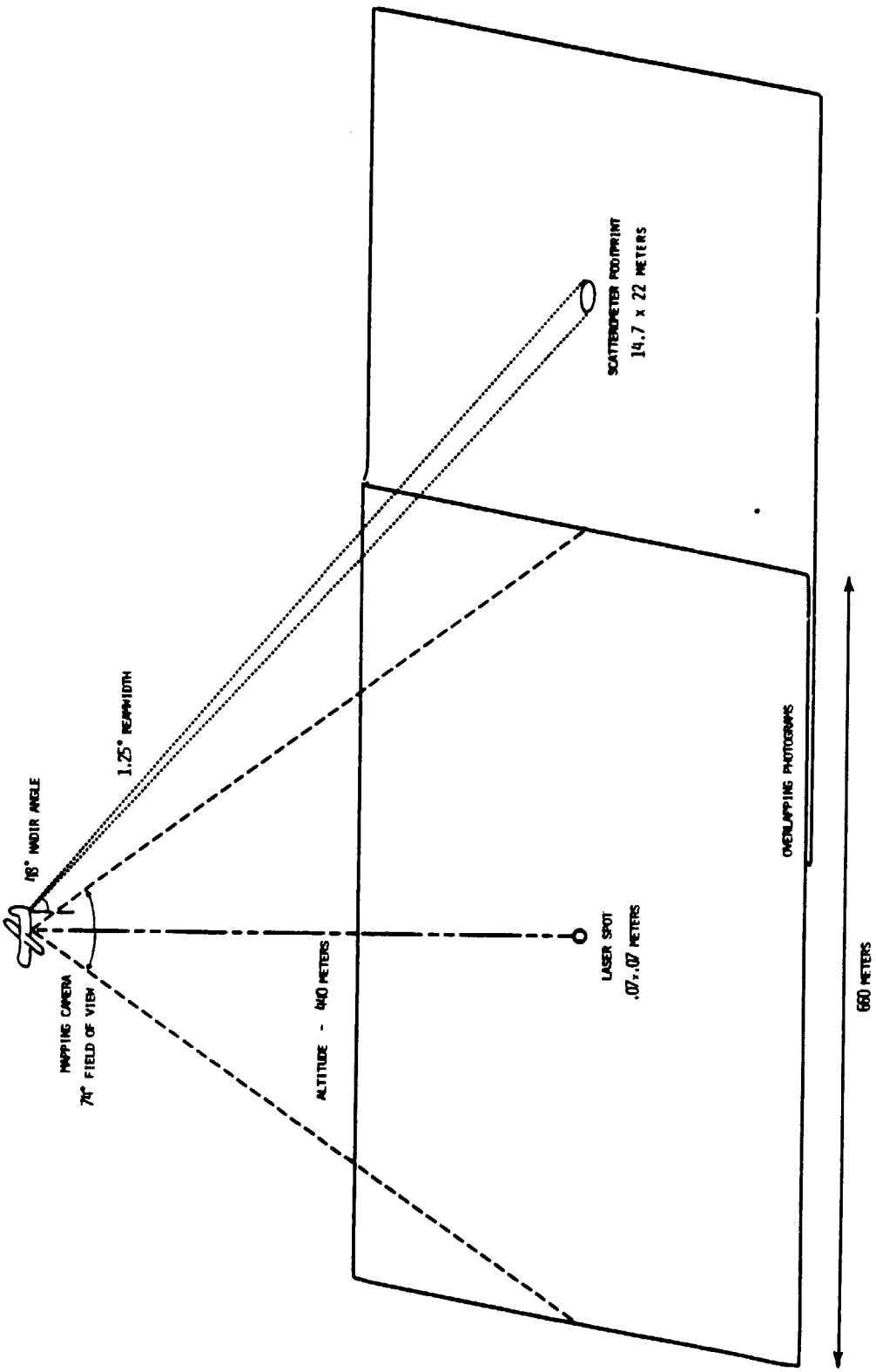

Figure 2.2. Relative Locations of Instruments' Illumination Areas

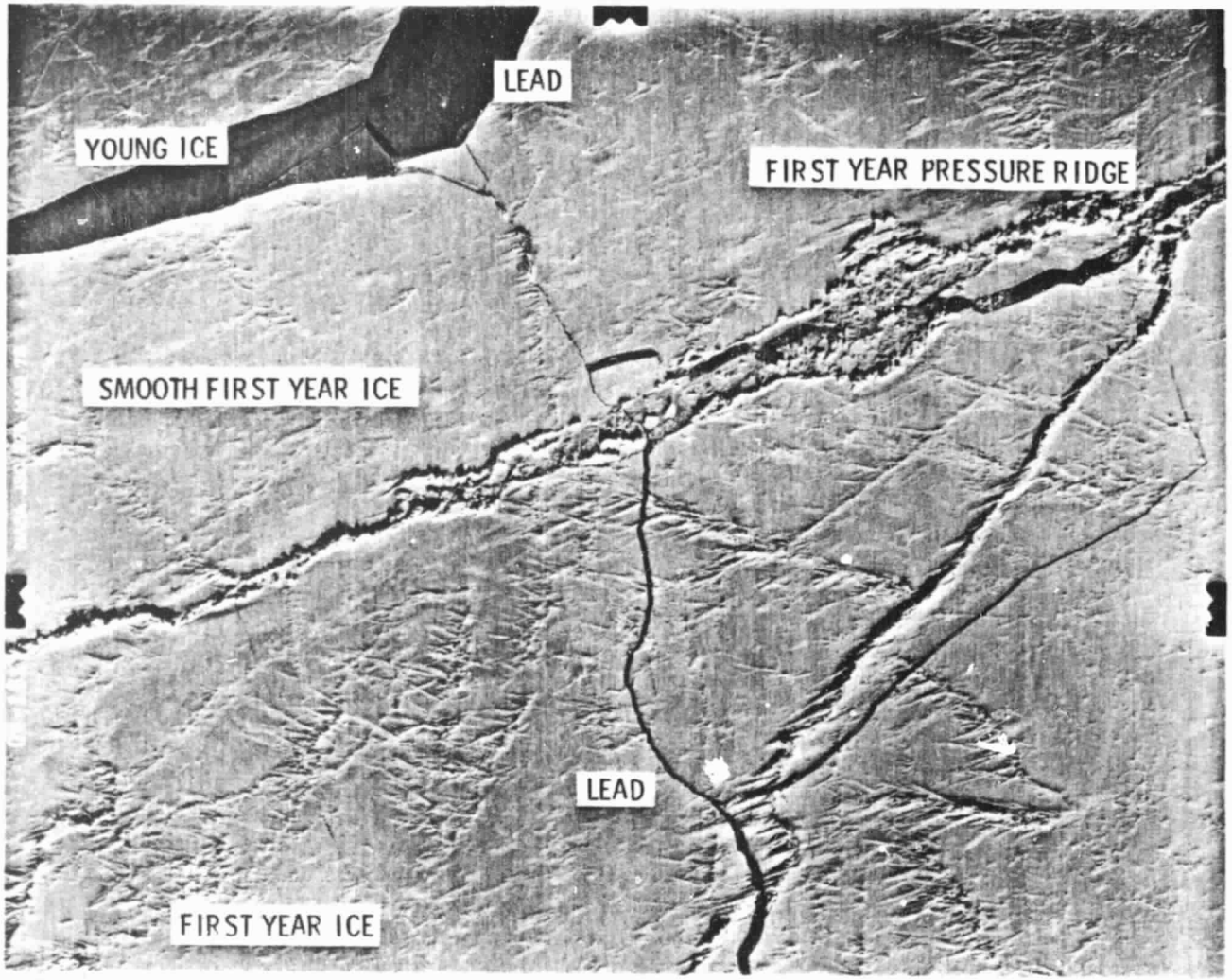

Figure 2.3. Facsimile of Aerial Photogram with Young Ice. Photo #04-181 NASA JSC 375, courtesy NASA Langley Research Center

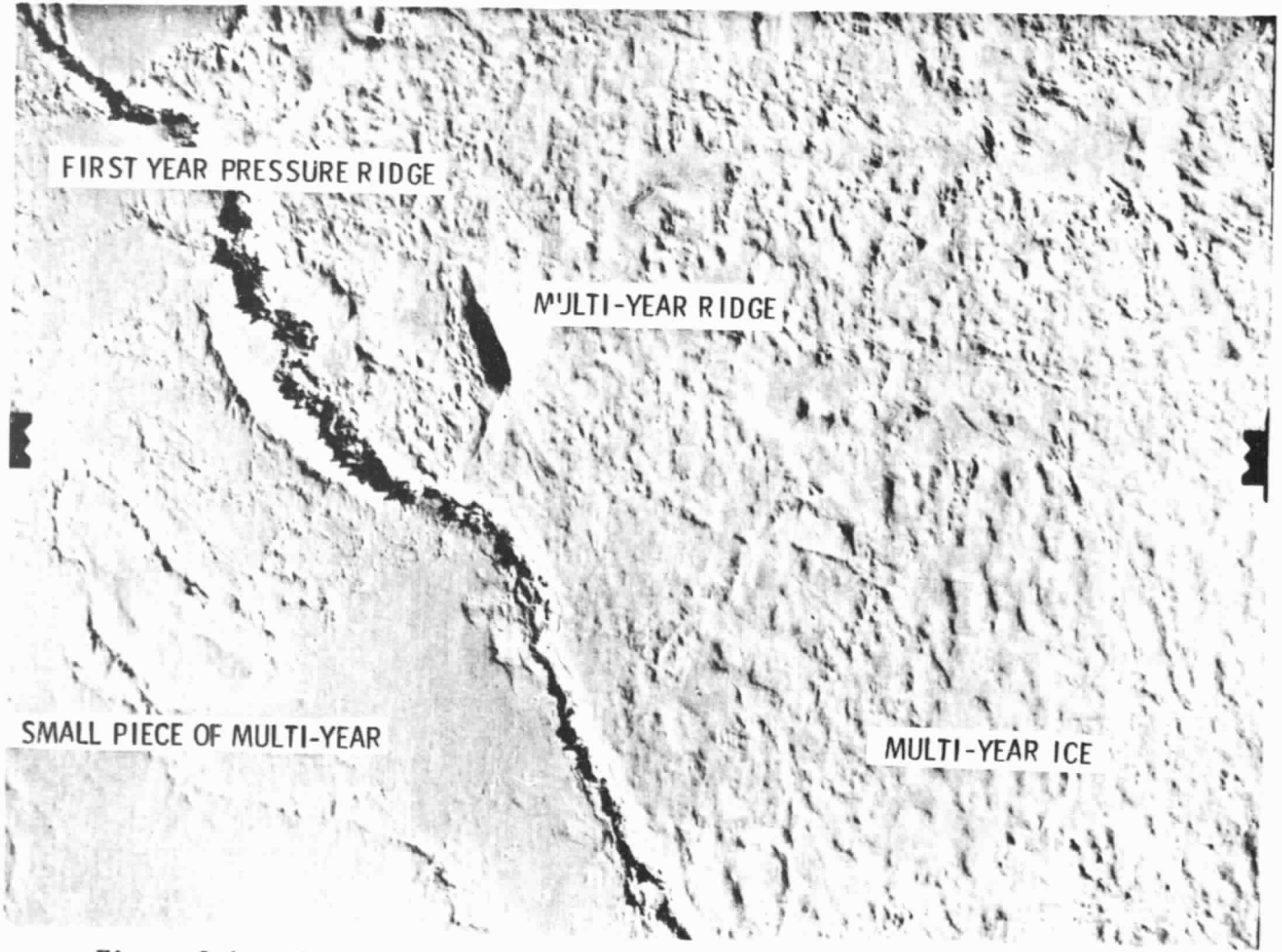

Figure 2.4. Facsimile of Aerial Photogram with Multi-year Ice.
Photo #10-031 NASA JSC, courtesy NASA Langley Research Center

differentiated from thick first year ice because the former has a smoother, weathered and wind worn appearance.

Because of its increased accuracy, photogrammetry is used in various remote sensing experiments to provide the comparison data set ("surface truth") against which instrument responses are compared. Recent studies between data collected by surface based methods and photogrammetric data of the same areas have shown that even the experienced ice observers in surfaced based camps consistently overestimated the ice concentration and amount of ridging by 15-20%, and exaggerated the areas of older ice by up to 40% [2].

The aerial mapping camera used during SIRE was the Zeiss RC-9 with a 6" focal length and a 74° field of view. This provided a ground coverage distance of 1.5 x the altitude (or 450 m at an altitude of 300 m). Photograms were 9" square, black and white contact prints and were taken with 20-60% overlap to allow stereo analysis of the surface topography. First, the photograms taken with this camera were used to classify the ice by age and thereby eliminate all non-first-year ice from the data set; and secondly, they were used to verify that both the laser and the scatterometer were looking at the same features, even though their fields of view did not coincide. Also, stereo analysis was performed on a limited set of photograms to investigate the error introduced in estimating a two-dimensional ice ridging process using a one-dimensional model.

2.3 Laser Profiler

Another remote sensor, the laser profiler, has been used extensively from aircraft to provide quantitative data on ice roughness. The profiler, using a radio frequency modulated light beam, measures the phase delay between the transmitted and reflected beam and thereby determines the distance from the aircraft to the surface. Thus, when the aircraft flies at constant altitude (relative to mean sea level), the distance between the aircraft and the ice surface is a measure of the topography. Like the camera, the laser cannot penetrate clouds or fog and is therefore limited in its use for general ice monitoring. However, it has served ice scientists well in the past by providing the ice topography over extended areas.

The profiler used in the SIRE missions was a Spectra Physics Geodolite Model 3A, (Figure 2.5), which contained a helium-neon laser (6328 A°) and a 8" telescope [14]. The instantaneous nadir-looking (0° incidence) laser spot diameter was 7.5 cm at 300 m altitude; but the effective along-track resolution was degraded to 1.4 m (for typical velocity) due to the distance traveled by the aircraft during the instrument's 20 ms integration period. The relative distance measurement accuracy was typically 3-10 cm for smooth ice [15]. However, errors could be significantly greater over ridges since ridges are comprised of piles of individual blocks of ice which can cause discrete distance steps rather than a continuous change in surface elevation. An analog output voltage proportional to relative

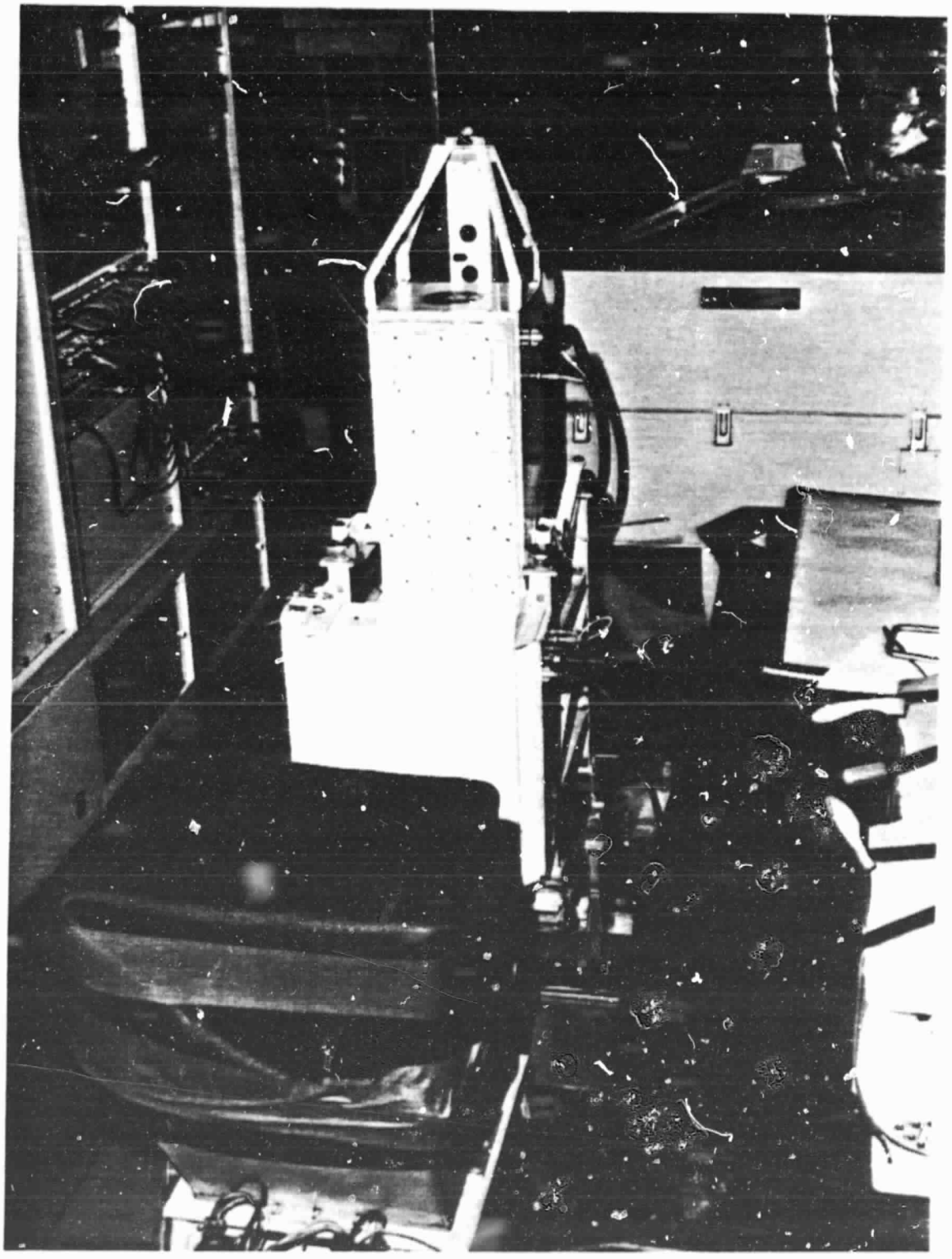

Figure 2.5. Laser Profiler, shown mounted in camera bay of C-130, courtesy NASA Langley Research Center

height (typically 40 foot full scale) was digitized at 100 Hz; and after some preprocessing, which will be discussed later in the chapter, these heights were used as the sole input to the model.

2.4 Microwave Scatterometer

A microwave scatterometer is an active (RADAR) instrument which measures the absolute backscattered power from a target. When this target is a surface of uniform scattering statistics, the use of the radar equation (see Appendix A) permits calculation of the surface reflectivity expressed as the normalized radar cross section, σ^o.

The scatterometer was first used over ice in 1969 by Rouse [16], who determined that it could be used to categorize sea ice based on age. The early success encouraged continued investigation, and it is presently known that σ^o is a function of the electromagnetic parameters frequency, polarization and incidence angle, and of the ice parameters salinity, temperature and roughness [17,18].

The scatterometer used in the SIRE missions was the NASA Advanced Applications Flight Experiment Radiometer/Scatterometer (AAFE RADSCAT) [19], shown mounted in the aircraft in Figure 2.6. It operated at 13.9 GHz, transmitted a horizontally polarized signal, and received horizontally polarized backscatter at an incidence angle of 48°. The RADSCAT had a "pencil beam" antenna of beamwidth 1.25°, which, for altitudes of 441 m and 48° incidence angle, provided an instantaneous footprint on the surface of approximately 15 m x 22 m. The RADSCAT used an "integrate and dump" method of data collection,

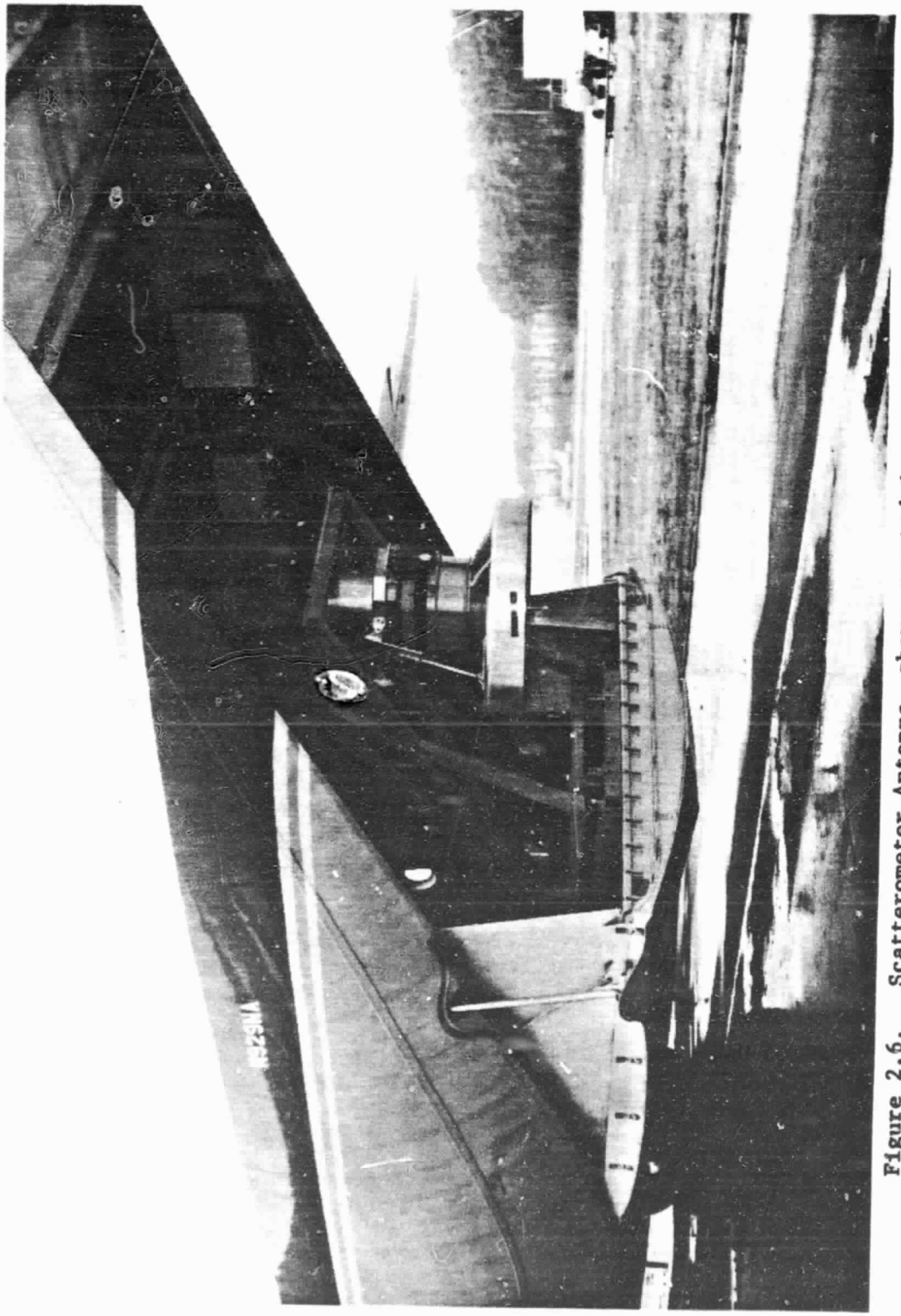

Figure 2.6. Scatterometer Antenna, shown mounted in cargo bay of C-130, courtesy NASA Langley Research Center

integrating for 100 ms, which corresponded to the Nyquist spatial sampling for the antenna footprint. This integration yielded a "smeared" footprint of 15 m x 29 m. Specifics on the instrument characteristics for the RADSCAT can be found in Appendix A.

The data from the scatterometer are used as the comparison data set for correlation with the model's predicted power. Once again, if the two data sets are highly correlated, then we can conclude that the scatterometer is a useful sensor for the identification of ice ridging.

2.5 DATA

This section discusses the differences between the instrument perspectives of the ice due to their differing nadir angles, and identifies how these differences will be handled. It defines how the data set was determined and discusses the processing of the laser data which was necessary prior to using it in the model.

2.5.1 Differences Between Instrument Perspectives

As can be seen in Figure 2.2, the nadir-looking profiler and the aft-looking scatterometer have different perspectives of the ice. In addition to their different spatial resolutions, the sampling rates are not the same, and their footprints are of different magnitudes. The laser's integrated spot size is 0.07 m x 1.4 m, while the RADSCAT's is 15 m x 29 m. Thus, the RADSCAT measures scattering from a two-dimensional area but the laser, because of the small width of its spot, effectively sees a one-dimensional view. The effects of

these differences must be compensated for in the model or be considered in interpreting results.

The difference in the viewing angle can be eliminated by rotating the coordinate system of the laser. It can be shown that this can be accomplished by adding the incidence angle of the scatterometer to the surface slope as determined from the laser. The difference in the sampling rates and spot length is accounted for in the model by a weighted averaging of the laser data to approximate the scatterometer's footprint length (alongtrack). The consequences of using a one-dimensional representation of a two-dimensional scattering process will be discussed with the conclusions in Chapter Five .

2.5.2 Data Selection

The data set was established by locating on the photograms the footprints for the laser and the RADSCAT, and then making subjective judgments that both sensors were "seeing" the same feature. The times for the areas used in this analysis were approximated from the photograms and identified exactly from the time series records of each sensor. Minor time adjustments were made between the laser and the scatterometer by matching dominant features in each time series. This was necessary for two reasons: each sensor was recorded using a separate time reference and, more importantly, the separation distance (time) between the sensor footprints was variable along the flight line because of changes in the aircraft attitude (roll, pitch, and yaw), ground speed and altitude.

For our analysis, all experimental measurements have been edited to select those data for which the degree of ridging is the only significant parameter. All areas studied are strictly first-year ice as identified by photo-interpretation; they are, therefore, similar in salinity and thickness. Data from different years were obtained in the same general location and under similar ambient conditions as measured by on-board sensors and are believed to be as identical as data from first year ice along different flight lines in the same mission.

Further, while it is possible that older first year ridges may be slightly less saline than the surrounding flat ice (because of leeching and ablation), it is not believed that this minor change in the ice dielectric properties is sufficient to affect the measure of σ^c significantly [20]. Only areas determined to be relatively free of loose snow were included in the data set. The electromagnetic parameters affecting σ^o were held constant by eliminating any data from the study set which were not at horizontal polarization or 48° incidence.

2.5.3 Surface Slope Processing

The input to the radar backscatter model is the mean ice surface slope over distances which are small compared to the spatial resolution of the scatterometer measurement. This mean slope was obtained from the laser profiler's signal which contained information on the ice topography. Unfortunately, the raw laser data also

contained instrument related artifacts (phase shifts) and distance changes due to aircraft vertical motion. Both of these perturbations had to be removed from the data prior to use in the model.

A phase shift occurs every time the relative distance goes through a full scale change (typically 40 foot scale). Figure 2.7 illustrates how the laser signal must change phase to keep the signal on its 40 foot scale as the aircraft changes altitude.

A phase shift was removed by adjusting all subsequent data by the amount of the shift, which is dependent on the scale setting and the direction and magnitude of the shift. Shifts can be 25%, 50%, or 100% of the scale setting. For instance, a 25% phase shift on the 40 foot scale would require a correction of ten feet.

Phase shifts are detected automatically by a program which computes the difference in magnitude between adjacent data points. Whenever this difference indicates that a shift has occurred, the subsequent data is increased or decreased by the precalculated amount. Since the ice surface does not change instantaneously by ten or more feet, there is little danger of editing out ridges with this program. Any jumps which are not detected by the program are removed by hand input corrections. Figure 2.8 shows the phase shift removed. It is obvious from the figure that missed phase shifts would be quickly noticed in the data.

Aircraft altitude changes are reflected in the laser data since the laser measures the distance between the aircraft and the surface.

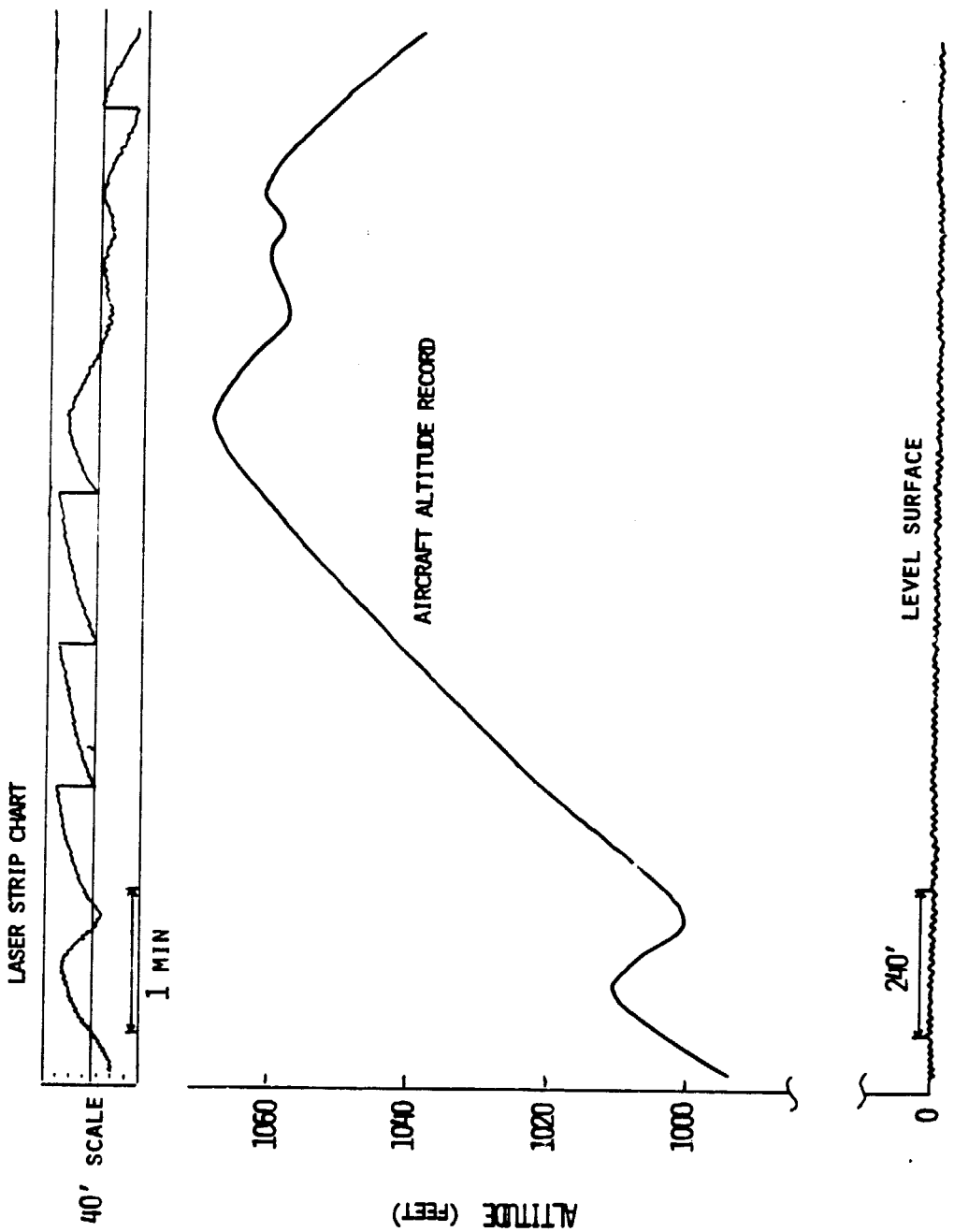

Figure 2.7. Physical Representation of Phase Shift

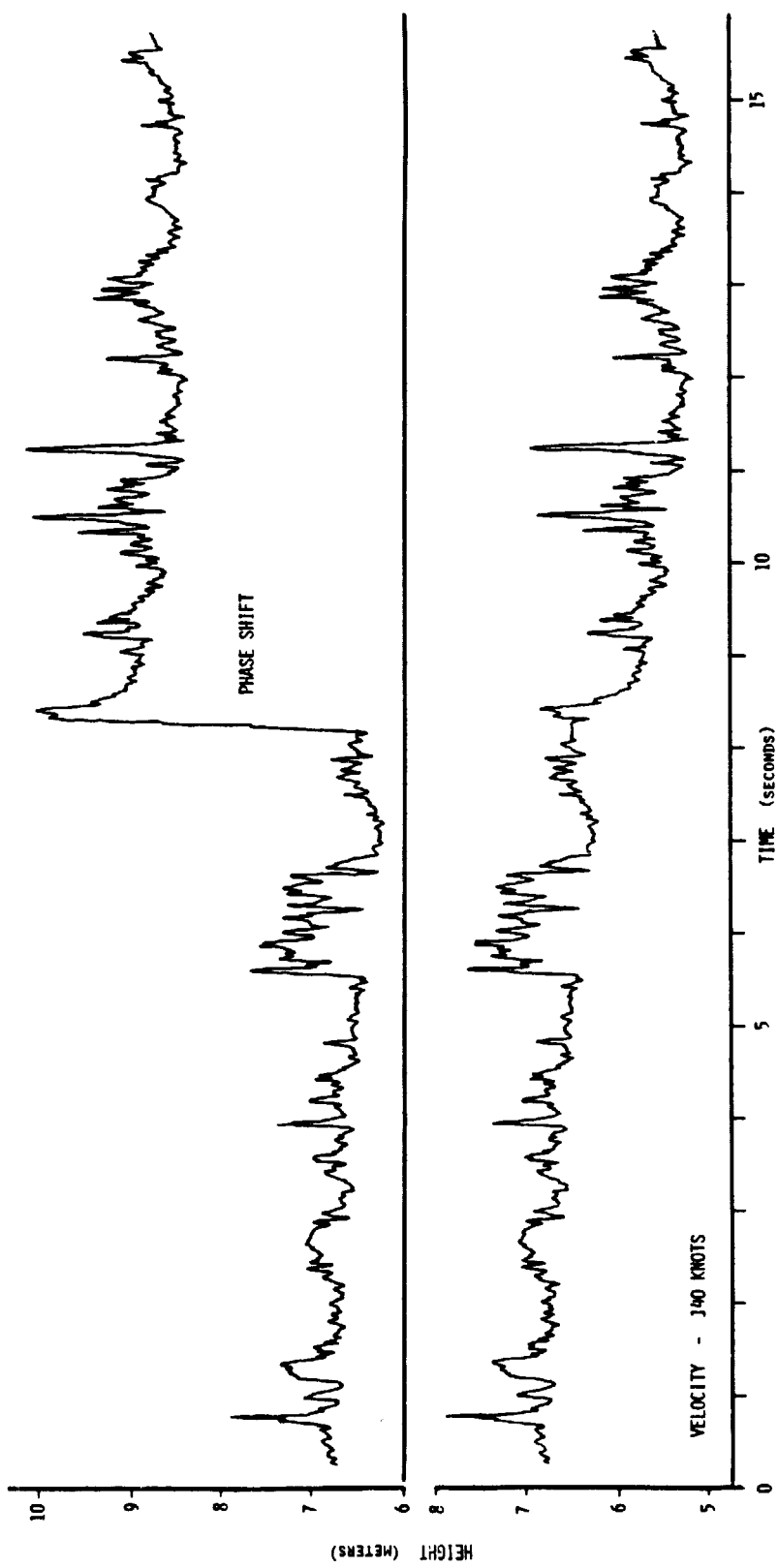

Figure 2.8. Removal of Phase Shift from Data

Figure 2.9 illustrates the aircraft motion in the data. These slowly changing oscillations in the data could ideally be removed by a high-pass filter. Unfortunately, the spectra of the altitude change due to aircraft motion and of the ice topography overlap [21]; therefore high-pass filtering would also remove low frequency ice information, which would be unsatisfactory. Figure 2.10 shows the results of a high-pass filter attempt. Notice that the ridge sits in an artificial depression which affects the accuracy of the height measurement.

The process which is used for this editing is a modified high-pass filter and substitution process which provides more accurate ridge information. The laser data (Figure 2.11a) is first low-pass filtered to provide the first approximation of the aircraft motion, (Figure 2.11b). The filtered line is then subtracted from the original data and the magnitude of this difference is monitored. Whenever the difference is greater than one meter, a substitution is made for the original data. This modified line now has had all significant ridging removed and replaced with flatter segments (Figure 2.11c). The modified line is low-pass filtered once more to yield an improved approximation of the aircraft motion (Figure 2.11d). This second approximation is then subtracted from the original laser line to produce a flat and level sea level base reference for the surface profile (Figure 2.11e), which is the way we believe the ice freezes. The accuracy of this method could possibly be improved by a second iteration of comparison between the first and second approximations.

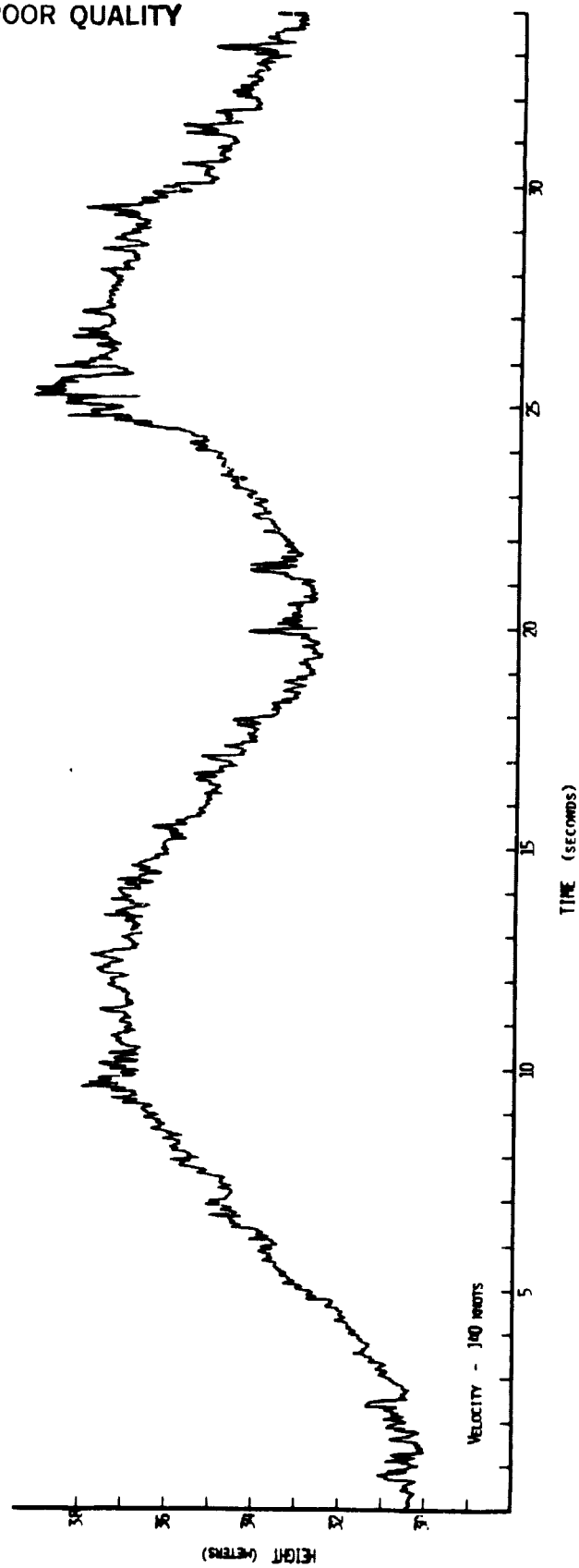

Figure 2.9. Aircraft Motion in Laser Data

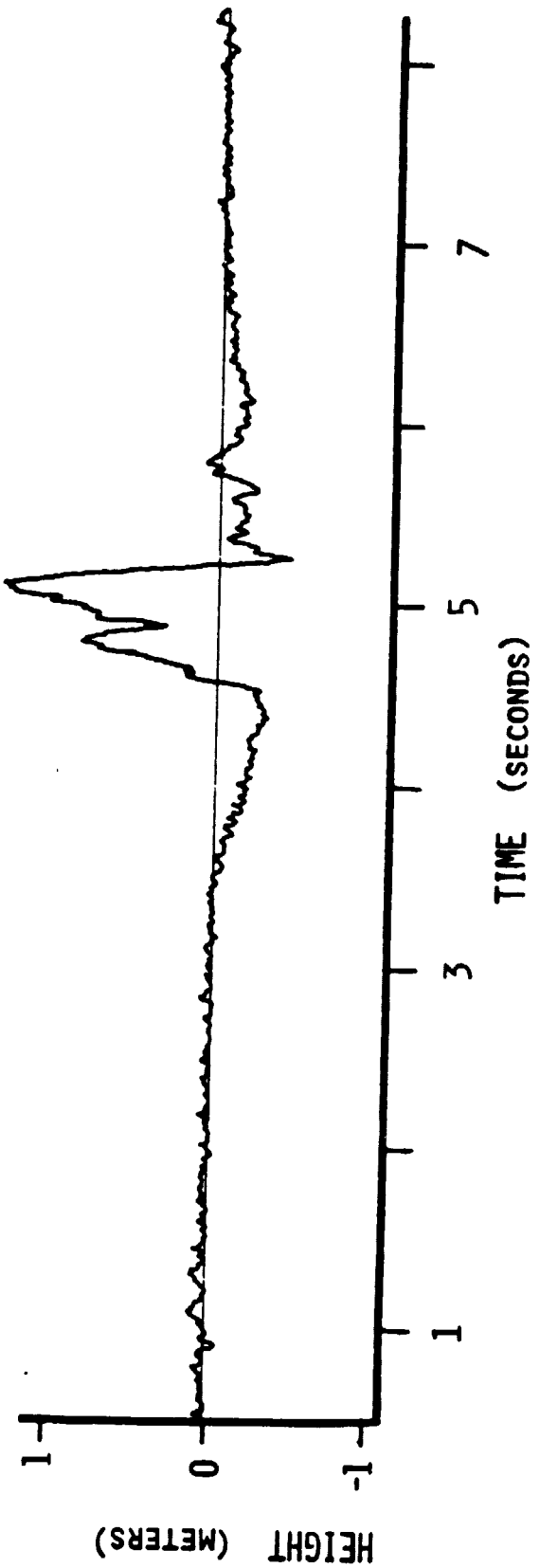

Figure 2.10. High-Pass Filter Attempt to Remove Aircraft Motion

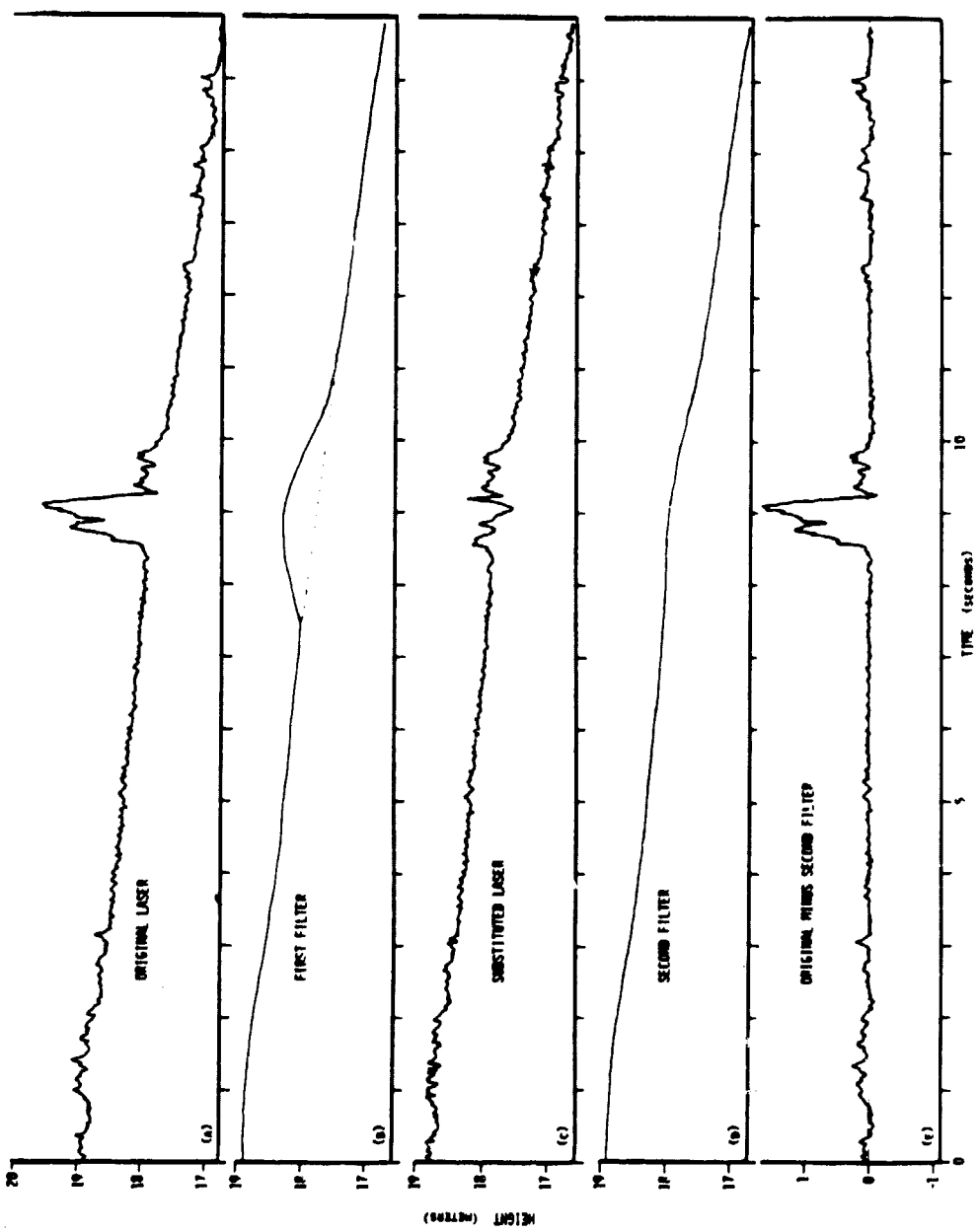

Figure 2.11. Aircraft Motion Removal

However, one substitution has provided an error of less than 5% of the ridge height which was felt to be within acceptable limits for our study. It should be pointed out that the slopes to be calculated later use a differential height between points and this error in relative height has even less than 5% effect on the slope.

At this point the laser data is ready for input to the model. The next chapter discusses the modeling process.

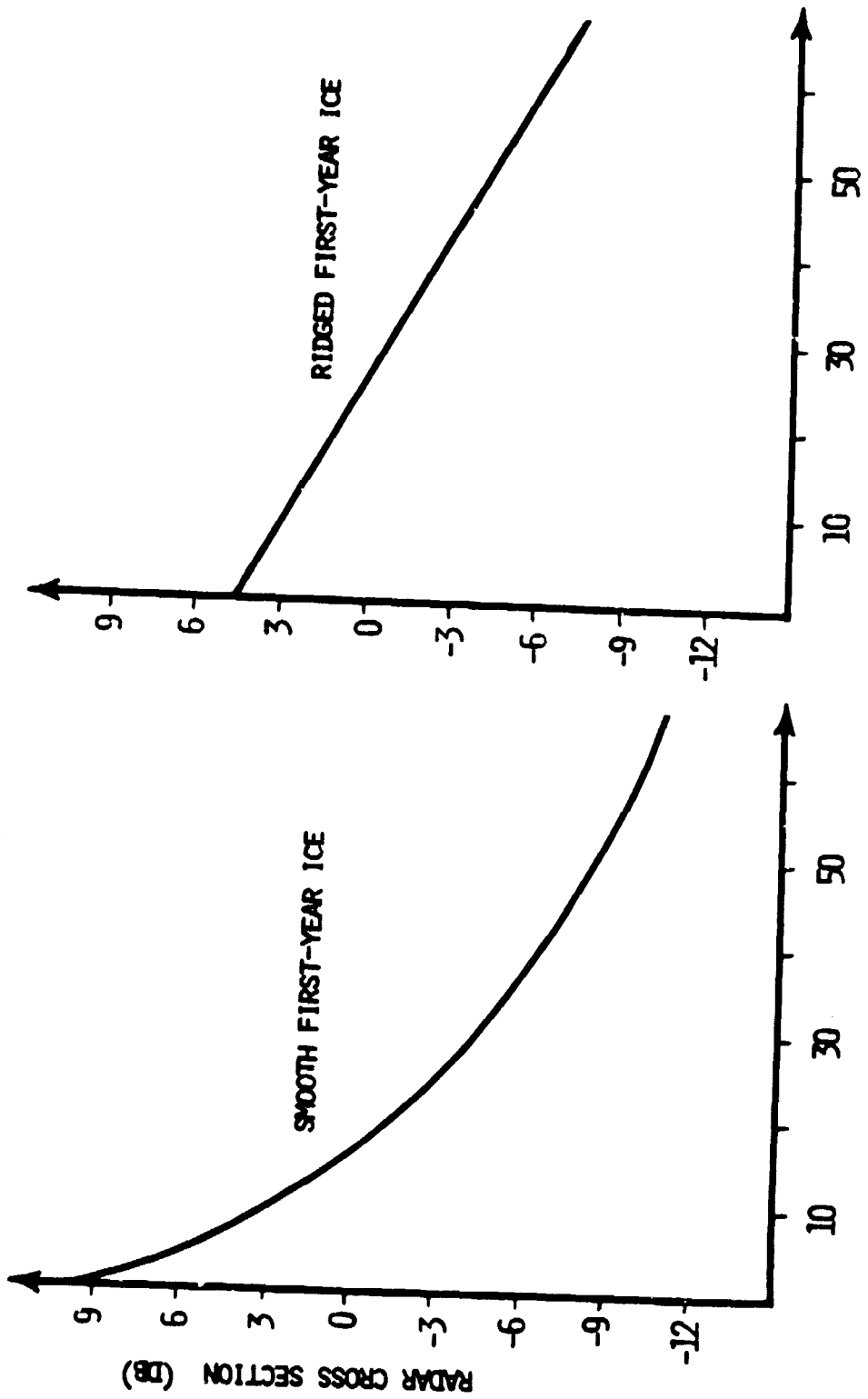

Figure 3.1. Onstott's Signature Curves

radar cross section, σ^o, as a function of the antenna angle, θ_n (the elevation angle of the antenna as measured from nadir). Since flat ice surfaces exhibit highly specular (non-diffuse) scattering, the strongest return occurs when the nadir angle is zero degrees (0^o), and the strength of the return signal decreases as the nadir angle increases, as illustrated in Figure 3.2. Note also from this figure, that for flat ice, $\theta_n = \phi$, where ϕ is the true incidence angle and is defined as the angle between the direction of propagation for the incident wave and the local normal to the surface. Figure 3.3 shows that for sloped surfaces, $\theta_n \neq \phi$, and in general, given the slope angle, α, of the surface,

$$\phi = \theta_n + \alpha \tag{3.1}$$

If ice ridges were simply smooth, tilted plates of ice, then their reflective characteristics could be determined from the signature for flat ice. However, ridges are not smooth, but are composed of blocks of differing sizes heaped together as the ice deforms. Figure 3.4 shows facsimiles of photographs of ridges taken on the ice surface, and Figure 3.5 is a facsimile of an aerial photogram of rough ice. Both figures illustrate the chaotic arrangement of the ice blocks. Given this roughness which occurs in ridging, and all the individual scattering faces, the assumption of specular scatter for ridged ice seems inappropriate. Thus, a different signature curve (shown in Figure 3.1) is used for our model for ridged areas. As before, the cross section, σ^o, decreases with increasing nadir angle, but here the slope is much shallower than that for flat ice.

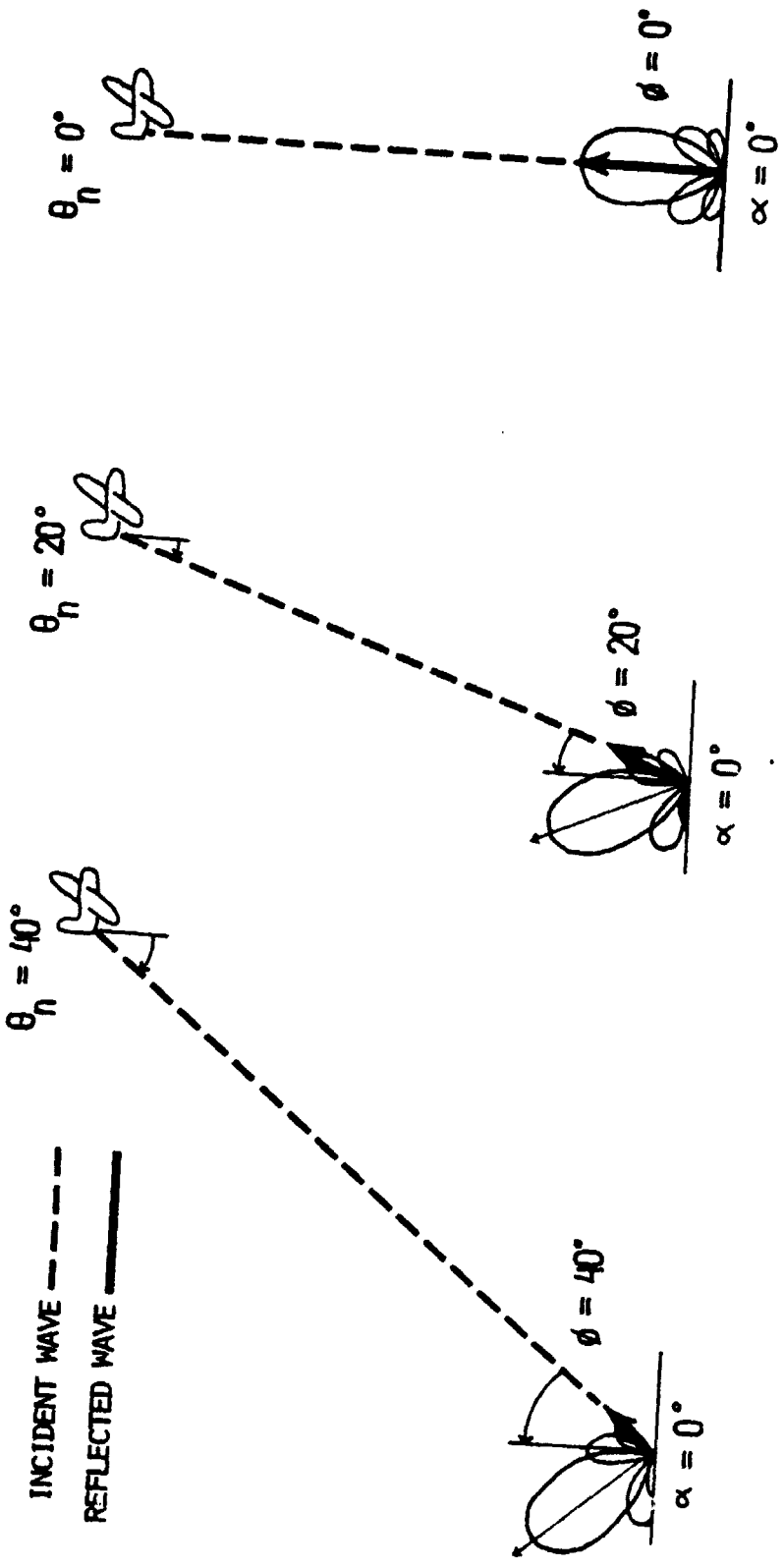

Figure 3.2. Illustration of the Relationship Between σ and θ_n for Flat Ice

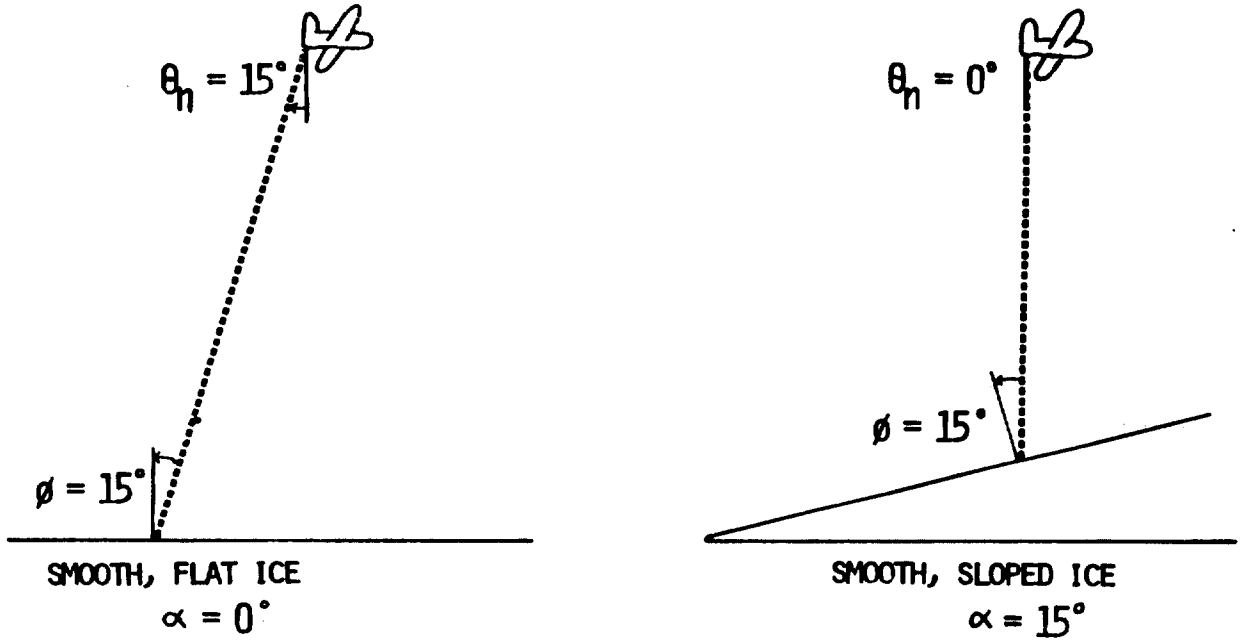

Figure 3.3. Illustration of Equal Return for $\theta_n \neq \phi$

Ridge height, 1.5 m, block thickness, 0.1 m

Ridge height, 2.0 m, block thickness, 0.4 m

Figure 3.4. Facsimiles of Surface Photographs of Ridges, courtesy US Army CRREL

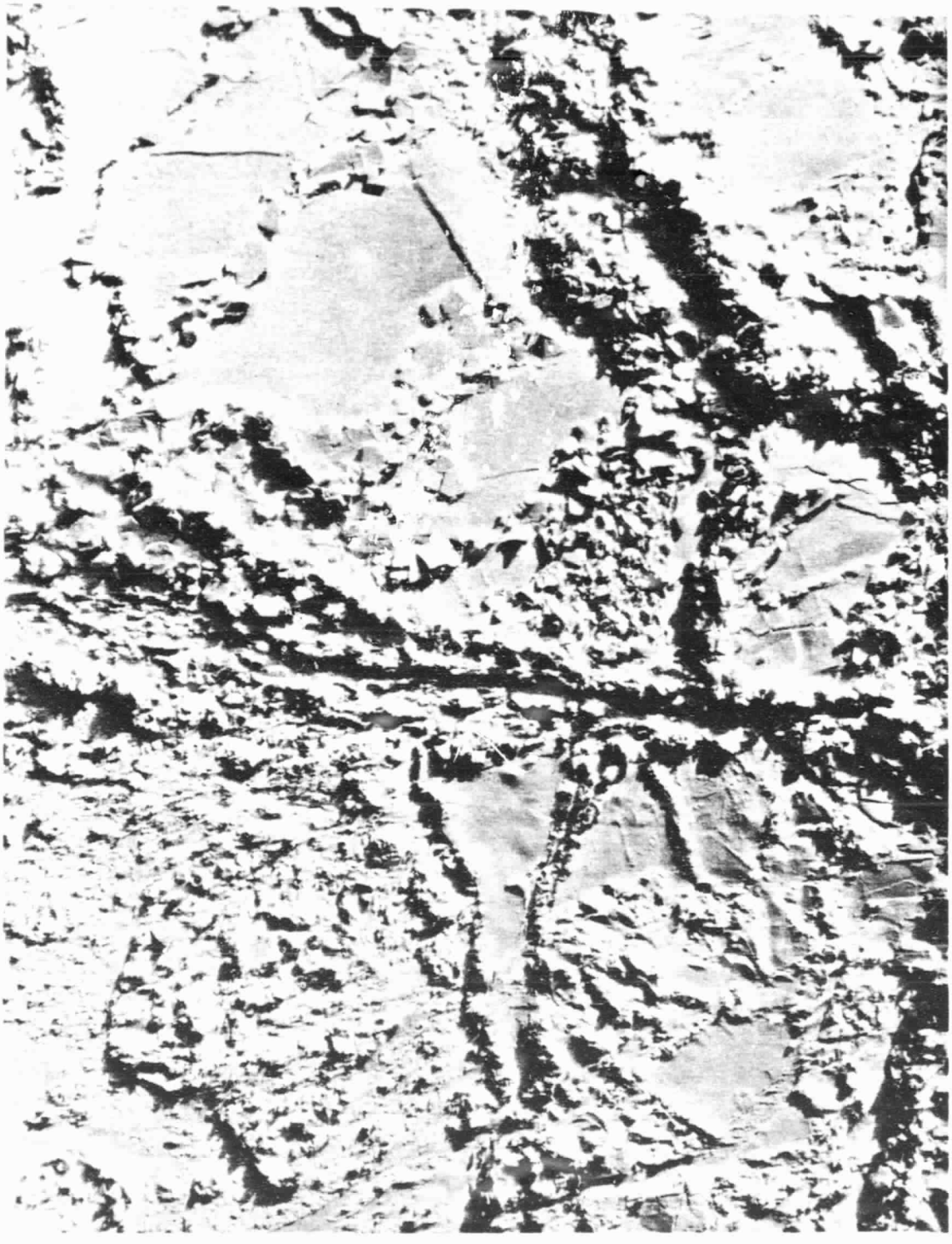

Figure 3.5. Facsimile of Aerial Photogram of Ridged Ice, Photo #05-370 NASA JSC 396, courtesy NASA Langley Research Center

3.3 Backscatter Model

We see from the signature curves in Figure 3.1 that the strength of radar backscatter, σ^o, is a function of the ice surface roughness and the nadir angle of the antenna. The other surface parameters which are known to affect σ^o, such as age, temperature and salinity, are held constant by editing the data selected for this investigation, as discussed in Chapter Two. Also, since the nadir angle for the RADSCAT measurements during SIRE was constant at 48^o, the radar cross section for these regions of first-year sea ice should be a function of surface roughness only. Therefore, it is this information which is used as the input to the model to calculate the radar return.

For this thesis the surface roughness is provided by the laser profiler. The radar backscatter model uses this one-dimensional representation of the ice topography and interprets it as subregions of slope (facets). Figure 3.6 illustrates how one scatterometer field of view incorporates many of these subregions, each of which has associated with it an incidence angle, ϕ, and a strength of return power, $\sigma[\phi]$, as determined from the signature curves. The total return power for a footprint can be determined by summing the partial returns from each of the facets.

The model is developed via several processes as shown in the flow chart in Figure 3.7. These processes can be broadly separated into the following: calculation of the incidence angle of each facet, $\phi(i)$; calculation of the return power from each facet, $\sigma[\phi(i)]$;

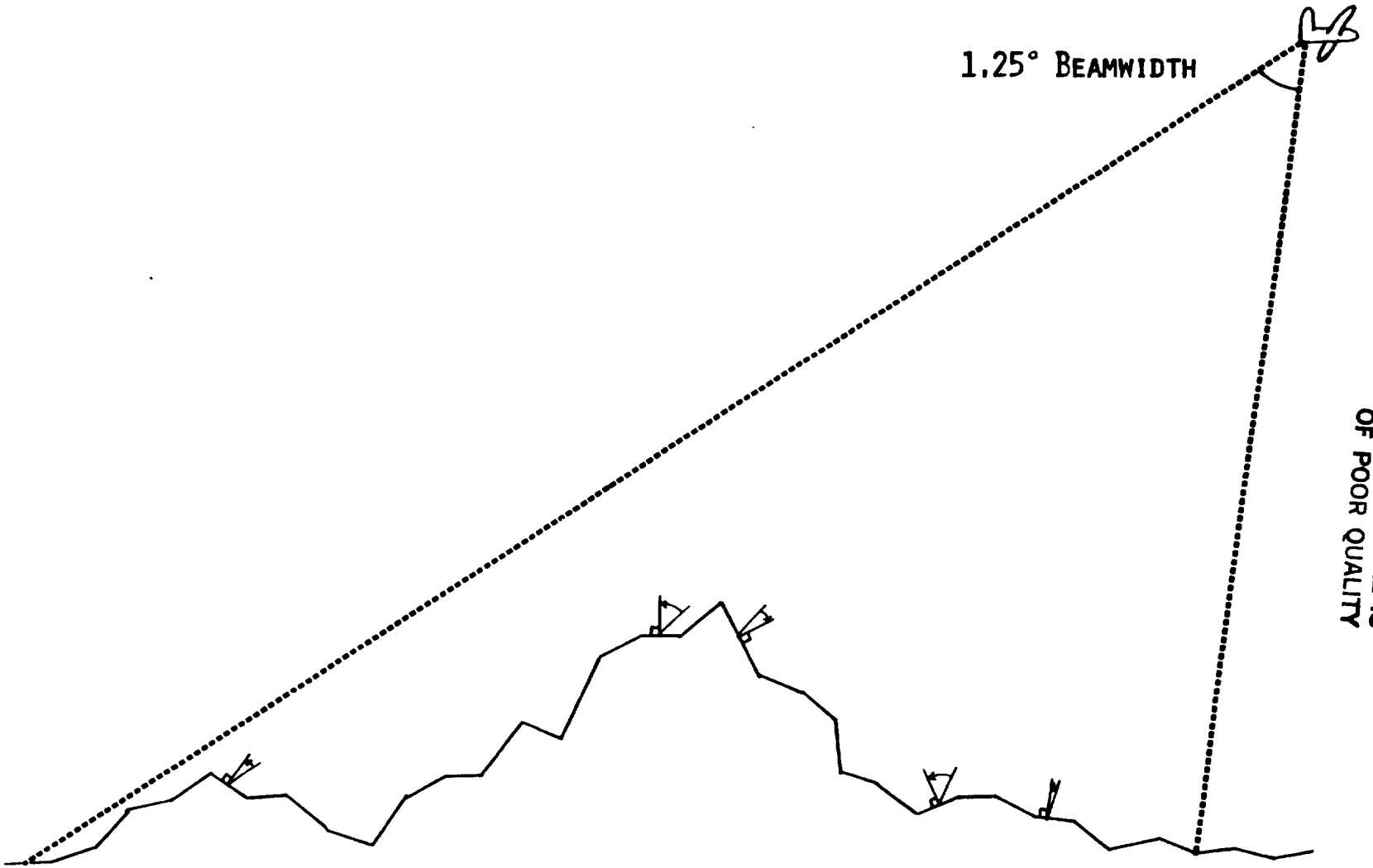

Figure 3.6. Illustration of Facets in Equivalent Resolution Cell

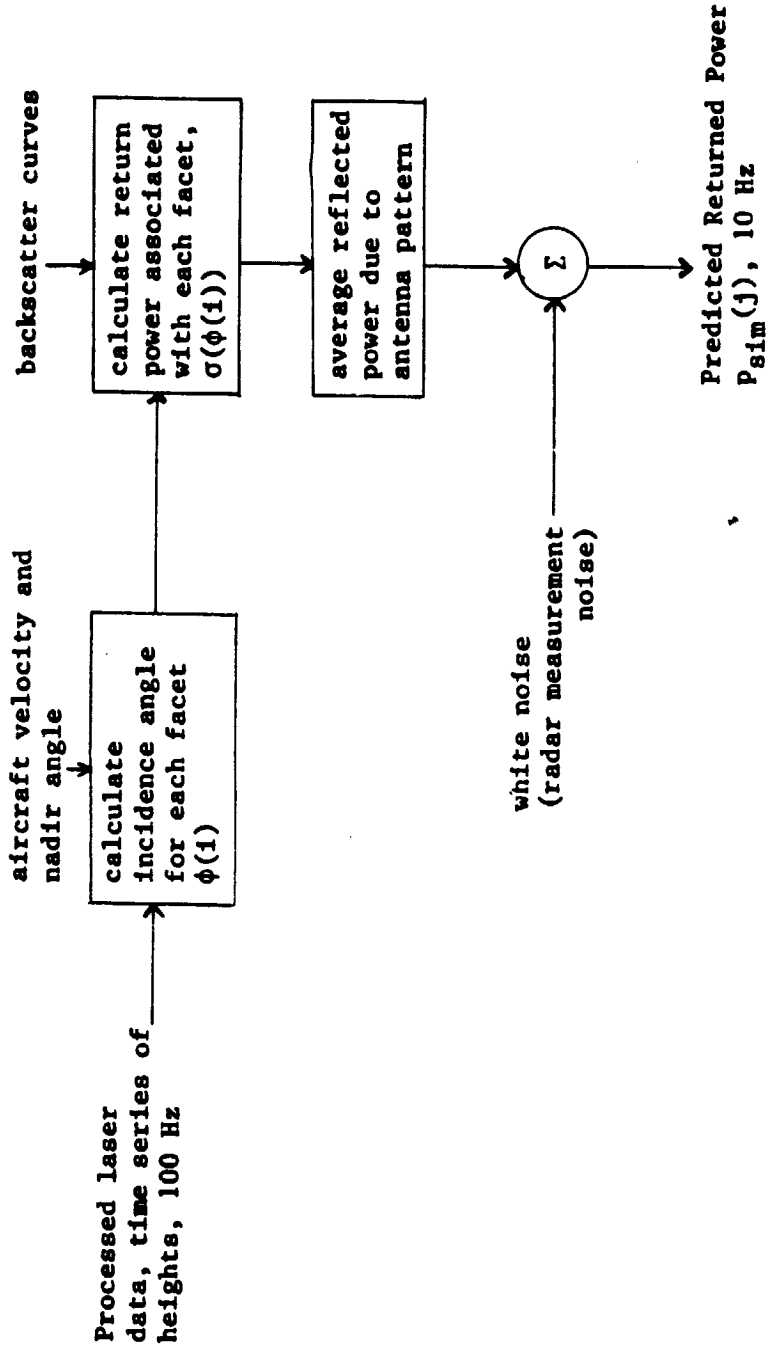

Figure 3.7. Flowchart of Modeling Processes

spatial and temporal averaging; and the addition of white noise (gaussian).

3.3.1 Calculation of Incidence Angle

Radar return, or backscatter, is a function of surface topography. The laser profiler data, after the preprocessing described in Chapter Two to remove aircraft altitude perturbations, provides this input to our model. The profiler produces a time series of surface height, h(i), above a mean sea level reference, as shown in Figure 2.11e. Knowledge of the aircraft velocity (148 knots) and the sample rate of the profiler (100 Hz) allows calculation of the horizontal distance, d, between samples. With these values, h(i), and d, the slope, α, of each facet can be easily determined by the equation

$$\alpha(i) = \arctan\left[\frac{h(i) - h(i-1)}{d}\right] \qquad (3.2)$$

In this way we have converted a sequence of height data in meters to a sequence of slope data.

The slopes, $\alpha(i)$, are not equal to the incidence angles, $\phi(i)$, since the scatterometer and the laser did not have the same nadir angle. Equation 3.1 can be used however, and for $\theta_n = 48^\circ$ we find

$$\phi(i) = \alpha(i) + 48^\circ \qquad (3.3)$$

This addition yields the same perspective of the ice surface that the RADSCAT had since it can be shown to be equivalent to the rotation of the laser's coordinate system. Figure 3.8 illustrates, for a simplistic view of a ridge, the incidence angles for a back face,

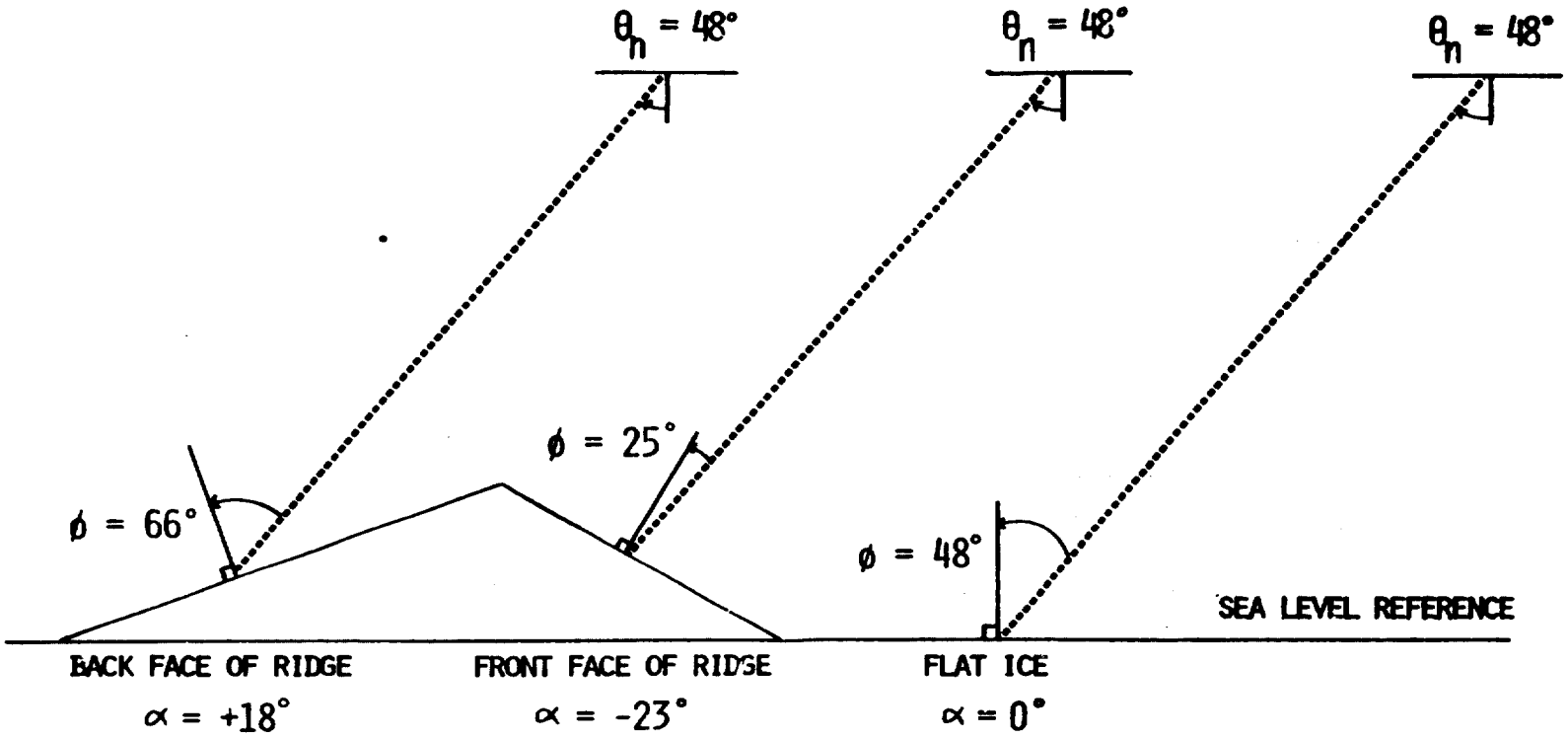

Figure 3.8. Illustration of $\phi = \theta_n + \alpha$

front face and flat ice as seen from 48° nadir angle. After the addition in Equation 3.3 we have a time series of true incidence angles, defined with respect to the RADSCAT's perspective, and still at 100 Hz.

3.3.2 Instantaneous Reflected Power Model

At this point we have an incidence angle, $\phi(i)$, associated with the i^{th} facet in the field of view, and we use Onstott's signature curves [22] (Figure 3.1) as the basis for determining the return power, $\sigma[\phi(i)]$, associated with that angle. The $\sigma[\phi(i)]$ are modified slightly from Onstott's in that they are a function of the incidence angle and not of the nadir angle. Secondly, they are linear rather than in dB since, as indicated in the flowchart, the values will be averaged. Neither modification alters the way the curves are used, but merely simplifies the calculations.

If the laser profiler had the same sample rate as the RADSCAT, as well as the same field of view, it would now be possible to compare the calculated returned power, $p_{sim}(i)$ (which at this point is proportional to $\sigma[\phi(i)]$), with the measured RADSCAT value, $p_{R/S}(i)$. However, neither is the same for both instruments.

To compensate for the difference in the fields of view we can average over the length of an instantaneous RADSCAT footprint all the $\sigma[\phi(i)]$ within that footprint. That is, since the instantaneous field of view of the RADSCAT is 22 m (altitude x beamwidth / $\cos^2\theta_n$) and the facets are 0.73 m (velocity / sample rate) apart, there are 30

facets within a given instantaneous footprint, as shown earlier in Figure 3.6. The reflected power from the surface illuminated by that instantaneous footprint could now be represented by

$$P_{sim} = \frac{1}{30} \sum_{i=1}^{30} \sigma[\phi(i)] \qquad (3.4)$$

Recall from Chapter Two that the RADSCAT does not yield instantaneous reflected power, but rather its output is the result of an "integrate and dump" measurement process. Thus, to calculate a returned power that is comparable to $P_{R/S}$ the averaging in Equation 3.4 is not sufficient. It is also necessary to average over the same integration period that the RADSCAT does. This takes us to the third process in the model.

3.3.3 Average Reflected Power Model

Since the aircraft is moving during the 100 ms that the RADSCAT integrates, it is not possible to deal with an instantaneous field of view, as was done in Equation 3.4. Rather, we must force the model to average all the facets which are in the smeared (integrated) area. Thus, we would expect the index in Equation 3.4 to increase, which it does. However, another factor must be considered--the radar antenna pattern. Like most antennae, the RADSCAT's does not have a uniform response across the footprint, so we perform a weighting of the facets, to simulate this pattern across the smeared footprint. One last manipulation of the data takes place before the power is averaged, and is done for the sake of simplifying the required

calculations. This last process divides the range of possible $\phi(i)$ values into 4° bins and calculates the percentage of footprint in each bin. Once again, a flowchart, shown as Figure 3.9, is used to organize these processes. They are: the equivalent resolution cell, antenna weighting, percentage area for each incidence range, and summing the power.

3.3.3.1 Equivalent Resolution Cell

In the 100 ms the RADSCAT integrates, the antenna has typically moved 7.3 m (velocity x integration time). This increases the illumination area to 29.3 m in length, or the equivalent of 40 facets. For all practical purposes, we can consider the time it takes the RADSCAT to clear the integrator to be negligible, and the next footprint area is immediately integrated. Figure 3.10 shows three consecutive footprints to illustrate the overlap which occurs on the ground. To simulate this, the model uses a "sliding" data window which processes 40 facets, slides the 10 facets equivalent to the 100 ms integration time, and then processes the next 40 facets. This could be expressed, assuming no antenna pattern effect, as

$$\rho_{sim}(j) = \frac{1}{40} \sum_{i=-19}^{20} \sigma[\phi(10(j+1)+i)] \qquad j=1,2,\ldots,N \tag{3.5}$$

The time series $\rho_{sim}(j)$ is now at 10 Hz, the sample rate of the RADSCAT.

AVERAGING FLOWCHART

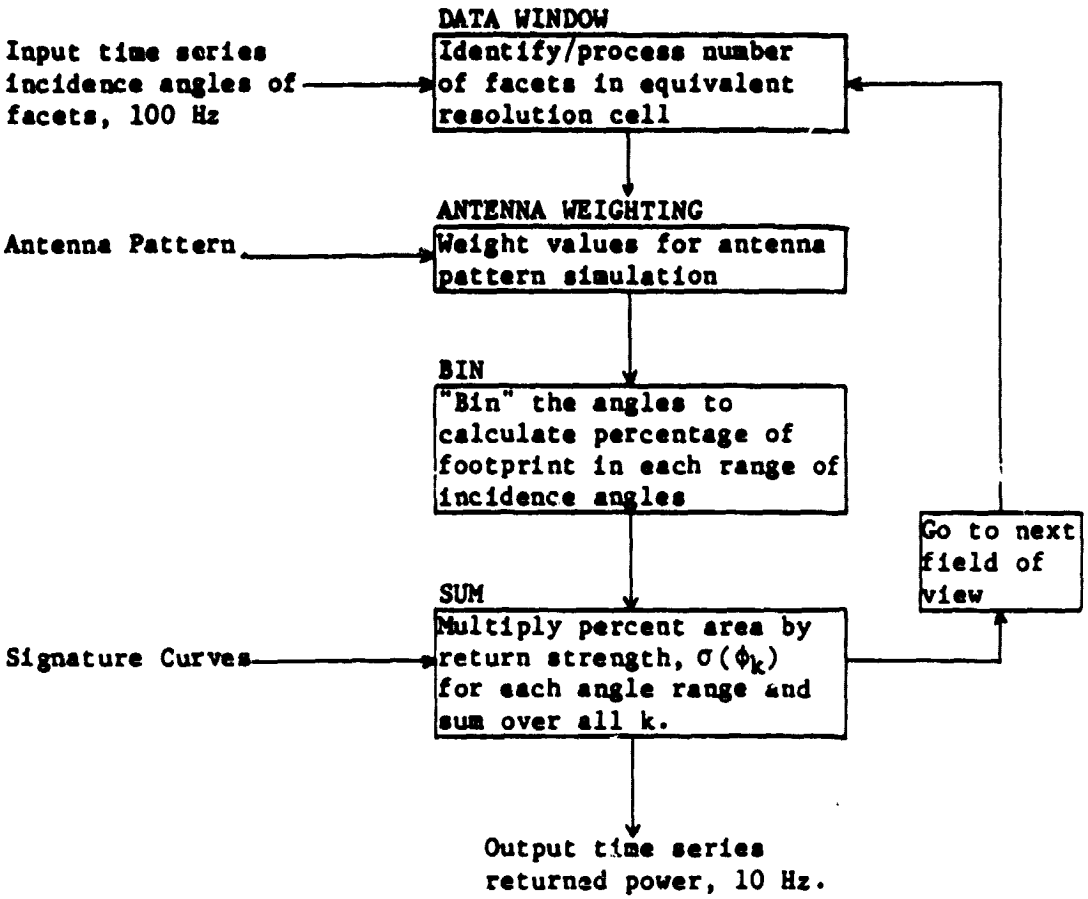

Figure 3.9. Flowchart of Averaging Processes

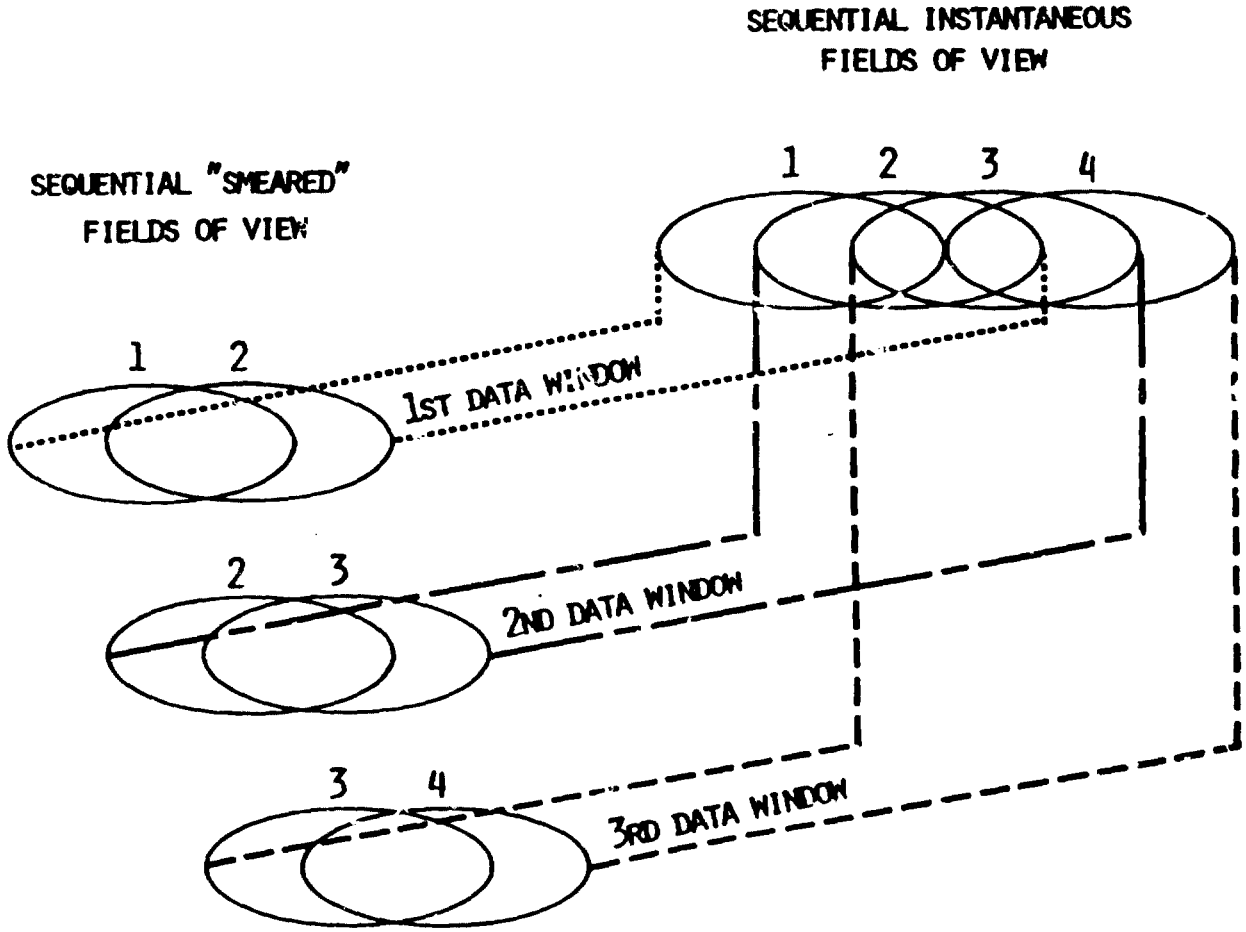

Figure 3.10. Illustration of Overlapping Resolution Cells

3.3.3.2 Antenna Weighting

The main beam radiation pattern for the RADSCAT is reproduced in Figure 3.11 [23]. Due to this pattern and the movement of the antenna during the integration period, the return power is more strongly influenced by the mid-region of the illumination area. To determine the weighting necessary to simulate these influences in the model, a convolution is performed. The integral which represents the reflected power is,

$$W(\theta) = \int_{-B/2}^{+B/2} G^2[\ \tau\ ]\ F(\theta - \tau)\ d\tau,$$

where $G(\theta)$ is the gain pattern (squared in the integral in agreement with the radar equation), $F(\theta)$ is the surface reflectivity as seen through a window of length B/3, and B is the 3dB beamwidth of the antenna. It is consistent with work previously established by Beck [24]. For the RADSCAT, the antenna pattern is approximated by

$$G(\theta) = 1 + (-1.6167)(\theta^2) + (1.0803)(\theta^4) - (0.2837)(\theta^6)$$

for $|\theta| < 2°$, and $F(\theta)$ is constant based on the small angle approximation that the variation of surface reflectivity with angle is negligible. The result of the graphical convolution is shown in Figure 3.12 and the continuous function $W(\theta)$ is approximated by the discrete weighting sequence, w_i, shown as a dotted line. The figure shows that a simple weighting is sufficient for the RADSCAT and amounts to doubling the power for the middle 20 values in the equivalent resolution cell. The returned power is now

$$P_{sim}(j) = \frac{1}{60} \sum_{i=-19}^{20} \sigma[\phi(10(j+1) + i)]\ w_i \qquad j = 1,2,\ldots \tag{3.6}$$

where $w_i = 2$ for the closed interval $i = [-9, 10]$, and $w_i = 1$

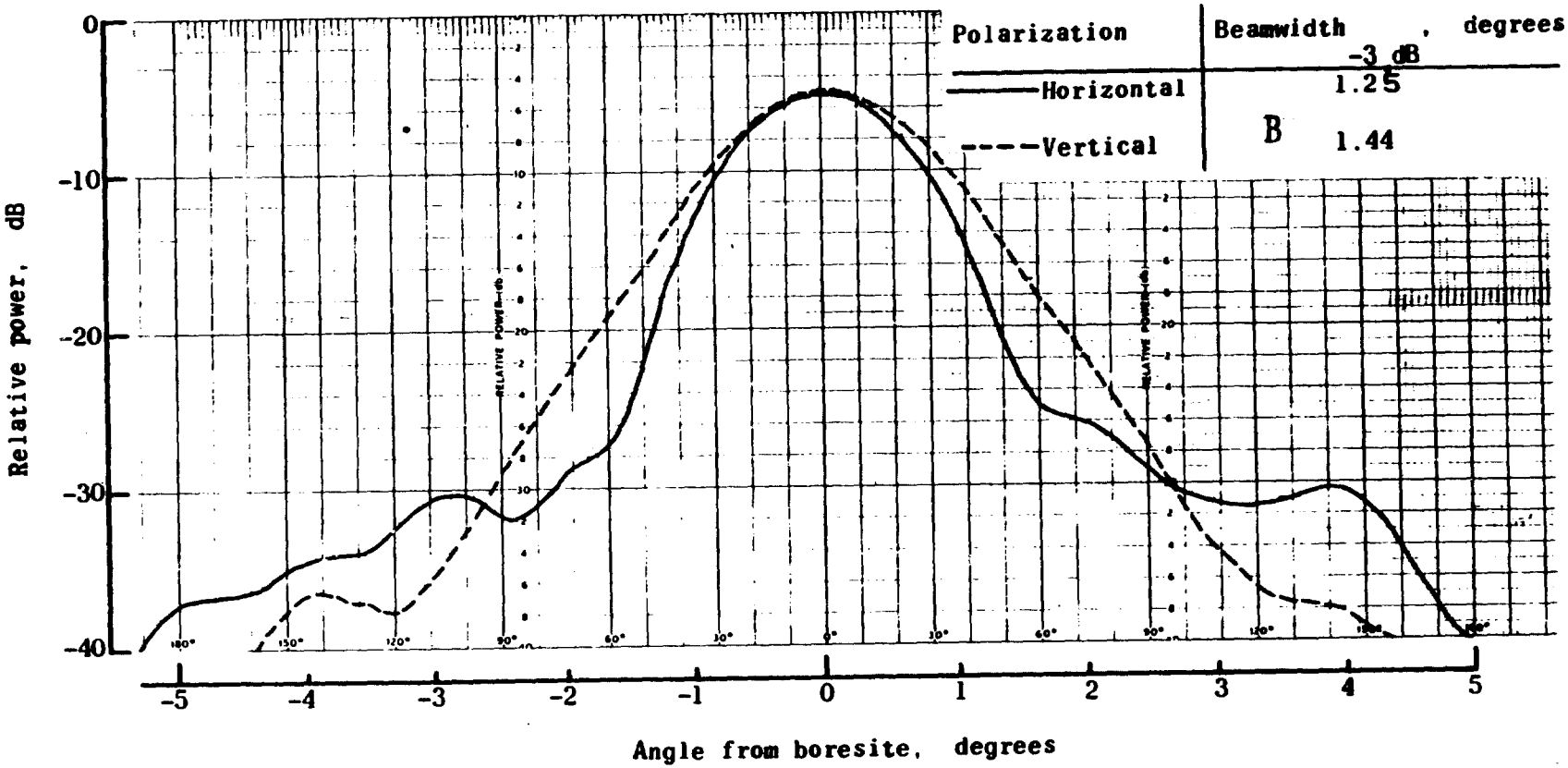

Figure 3.11. RADSCAT Antenna Pattern, main beam. Courtesy NASA Langley Research Center, NASA TMX-72844

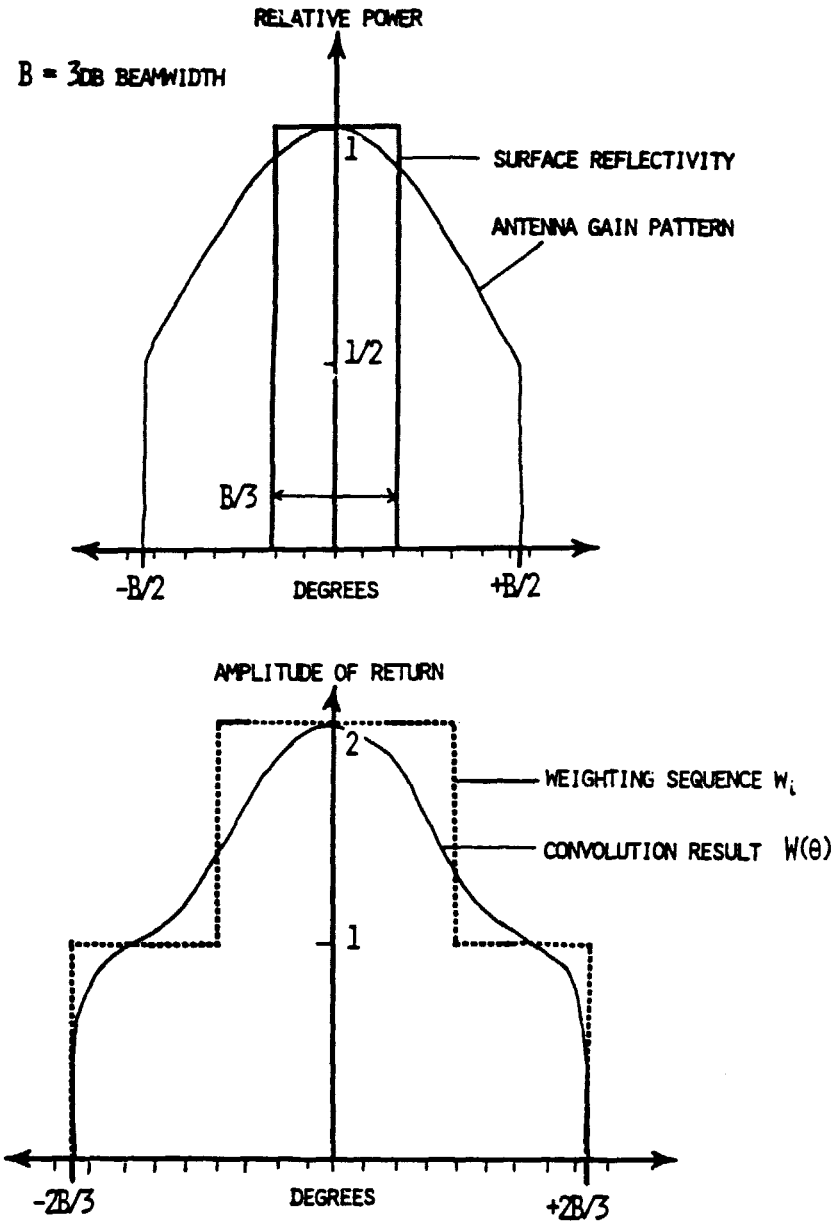

Figure 3.12. Illustration of Weighting Sequence

elsewhere. At this point the series $p_{sim}(j)$ could be compared with the measured sequence from the RADSCAT on a point-per-point comparison.

3.3.3.3 Calculation of Area

To simplify the calculations and because the slope of the signature curves is small, the range of $\phi(i)$ is divided into 4° subranges, or bins. Flat ice is defined as ice with less than $|2°|$ slope, i.e., an incidence angle between 46-50° . All other ϕ are defined as rough/ridged ice. There are k 4° bins.

To calculate the returned power for an equivalent resolution cell, we determine what percentage of the cell including the results of the weighting is in each incidence angle subrange. Once these percentages, p(k), are calculated, the return power for the cell is determined by summing the product of p(k) and $\sigma(\phi_k)$, where $\sigma(\phi_k)$ is the strength of return from the signature curve taken as the average value of σ over the k^{th} 4° bin. That is, for one equivalent cell, the modified calculation becomes

$$P_{sim} = \sum_{k} p(k)\ \sigma(\phi_k) \qquad (3.7)$$

3.3.4 Addition of Radar Measurement Noise

The signature curves provide $\sigma(\phi_k)$, which is the mean power for a surface. It is necessary that this model be capable of predicting the instantaneous value, since the RADSCAT measures the estimated mean power which has been corrupted by noise. If we want to predict the instantaneous power at the receiving antenna, we would add

Rayleigh noise, which would account for the fading statistics from the rough surface. If we are interested in the received power measured by the RADSCAT (at the output of the scatterometer), we would add white noise (gaussian) since a Rayleigh distribution becomes gaussian when it undergoes the square law detection and integration process. Since the comparison which needs to be made is between the calculated power and the measured power, the white noise which is added to the time series should have a gaussian distribution.

The noise added in the model had a zero mean, and a standard deviation of 0.317, as determined from the bandwidth and integration time for RADSCAT. After the addition of this noise, we have a time series which can be compared point-by-point with the measured values from the scatterometer. This comparison and the discussion of the results of the modeling effort will be presented in Chapter Four.

CHAPTER FOUR

MODEL SIMULATION

4.1 Introduction

This chapter presents simulation results of the backscatter model, and comparisons with RADSCAT measurements obtained during SIRE. The selected data was divided into two groups: a training set and an evaluation set. The processes for the model, as discussed in the last chapter, were used to calculate the simulated return, p_{sim}, and then the measured return, $p_{R/S}$, from RADSCAT was used to "train" the model. That is, using an iterative process, the various components of the model were adjusted using a least squares approach to minimize the difference between the calculated values and the observed backscatter values. Next, the refined model was compared to independent data in the evaluation set.

Also presented are the results of the stereo analysis which give insight into the two-dimensional nature of the ridged ice surface. The chapter begins with a review of the training and evaluation data sets selection.

4.2 Data Selection

Since the RADSCAT, laser profiler and RC-9 mapping camera were co-located on the same aircraft, it is possible to use the measured aircraft drift to locate the laser spot and RADSCAT antenna footprint on the aerial photograms. Drift, or yaw (the difference between the aircraft heading and course), was recorded by the on-board navigational system. By examining the traces of the footprints on the photos, a subjective decision was made to determine whether the laser, which tracked along the center of the photos, and the entire scatterometer cell were within an area homogeneous in roughness, i.e., seeing the same feature. Figure 4.1 shows an example of this process. Time was approximated from the photograms and determined exactly from the laser profile by feature matching. A number of areas were identified and selected for processing in this manner, giving us confidence that the degree of ridging was the same for both sensors.

4.3 Adjustment to $\sigma[\phi(i)]$

The radar backscatter signature curves shown in Figure 3.1 were derived by Onstott et al. [22], from ice observations at the same frequency and polarization as RADSCAT. The ordinate is σ°, the normalized radar cross section, measured in dB. To review the notation used, p_{sim} is the predicted total returned power for a given equivalent resolution cell, $p_{R/S}$ is the measured returned power from the RADSCAT for one resolution cell. Both are linear values of power. For clarity, whenever it is necessary to use

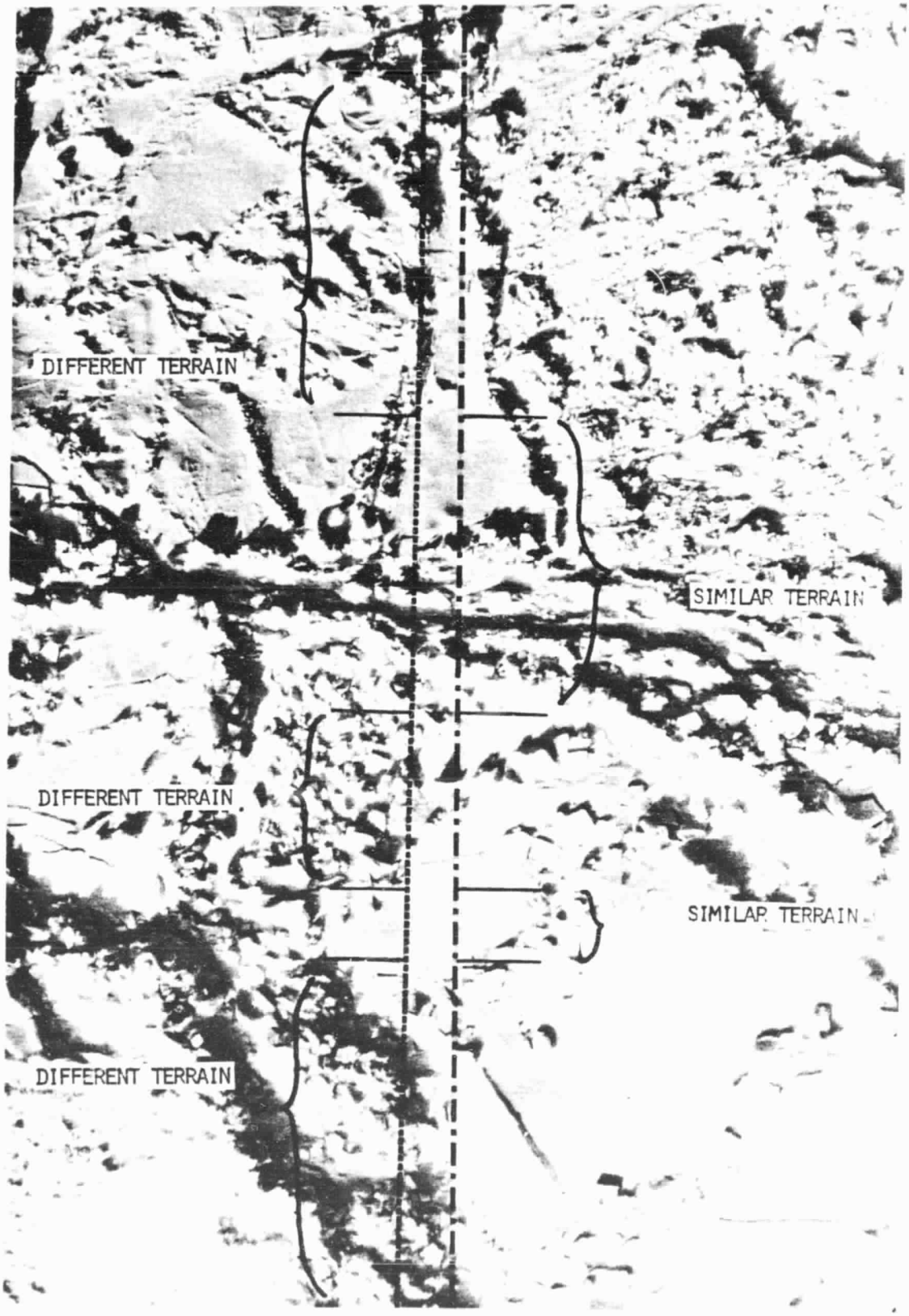

Figure 4.1. Selection of Data from Photogram

logarithmic values, they will be subscripted with dB. That is,

$$p_{sim\ dB} = 10 \log_{10} p_{sim}.$$

The term $\sigma[\phi]$ is the strength of return factor, determined from the σ° curve as a function of the incidence angle. It is used to calculate p_{sim} for this thesis, since an absolute $\sigma^\circ_{R/S}$ (σ° for RADSCAT) was not available. However, it was apparent after the first output of the model was analyzed, that p_{sim} was not of the same order of magnitude as $p_{R/S}$. The range of p_{sim} was 10-50 milliwatts, while the range of $p_{R/S}$ was 0-750 milliwatts. To normalize the simulated power to the measured power, it was necessary to find the proper scaling factor, m, and to scale $\sigma[\phi]$ by that factor. That is,

$$\sigma[\phi] = m \times \sigma^\circ[\phi]$$

To determine m, an equality was forced between σ° and $\sigma^\circ_{R/S}$ for smooth first year ice. The values for $\sigma[\phi]$ were then adjusted by m through the relation

$$\sigma[\phi] = 10^{[(\sigma^\circ_{dB} + \hat{m})/10]} \qquad (4.1)$$

where $\hat{m} = 10 \log_{10} m$.

4.4 Time Adjustment by Features

Because of the scatterometer geometry, that is, the 48° nadir angle, there is a delay of approximately six seconds between the times that the laser and the scatterometer view a particular feature. The time offset, t, can be calculated with the equation,

$$t = (\text{altitude} \times \tan 48^\circ)/\ \text{velocity}$$

Since, for given flight lines, the altitude and velocity were fixed, t is nearly constant, and the adjustment is easily made by using different start times in the computer program for each of the data sets.

Occasionally, a different type of time adjustment must also be made to correct for the aircraft drift when the ridges are not perpendicular to the flight track. When the aircraft drift is greater than 1.5°, the laser spot does not lie within the scatterometer footprint, and the two sensors cross the ridges at different points. Figure 4.2 illustrates the difference in the distance between ridges, for each sensor, when the ridges are not parallel to each other nor perpendicular to the flight track. Since the comparison between the simulated and the measured values will be done on a feature-by-feature basis, a time adjustment must be performed to prevent a degraded correlation. This correction is made by compressing or expanding, as necessary, the time frame between the ridge responses for the simulated values. This correction does not alter the magnitude of the response.

4.5 Adjustment to Signature Slopes

When the new p_{sim} time series, calculated using the scaled $\sigma[\phi]$ and after the time adjustment for features, was compared to $p_{R/S}$, it was determined that there was a need for further refinements to the model. Figure 4.3 shows the plot of the two time series. It is seen from the plot, that the simulated power is too low

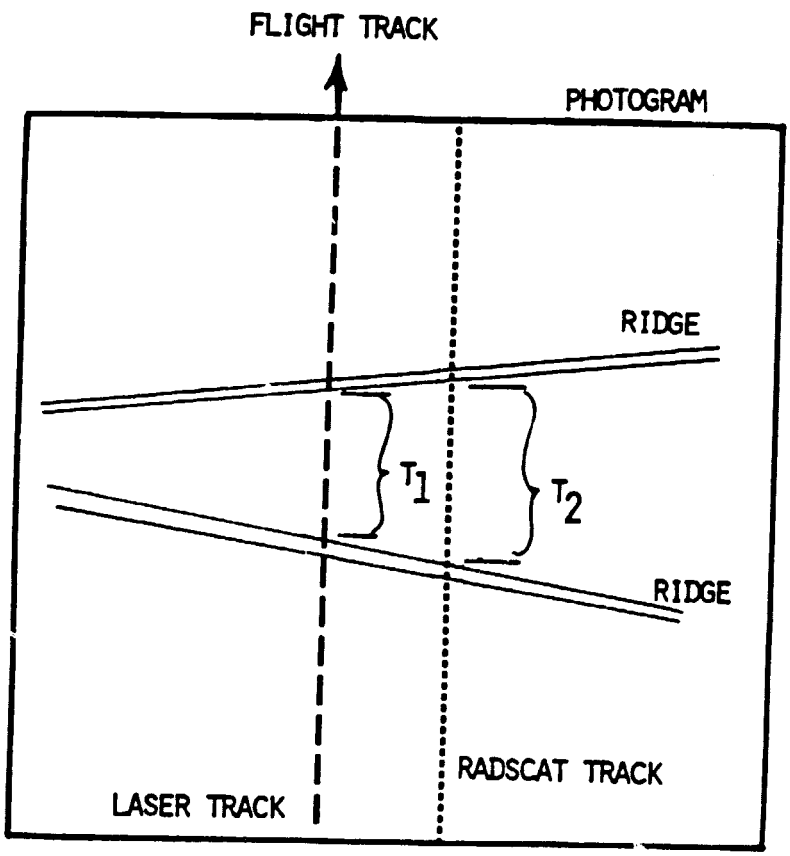

Figure 4.2. Illustration of Correction for Feature Alignment

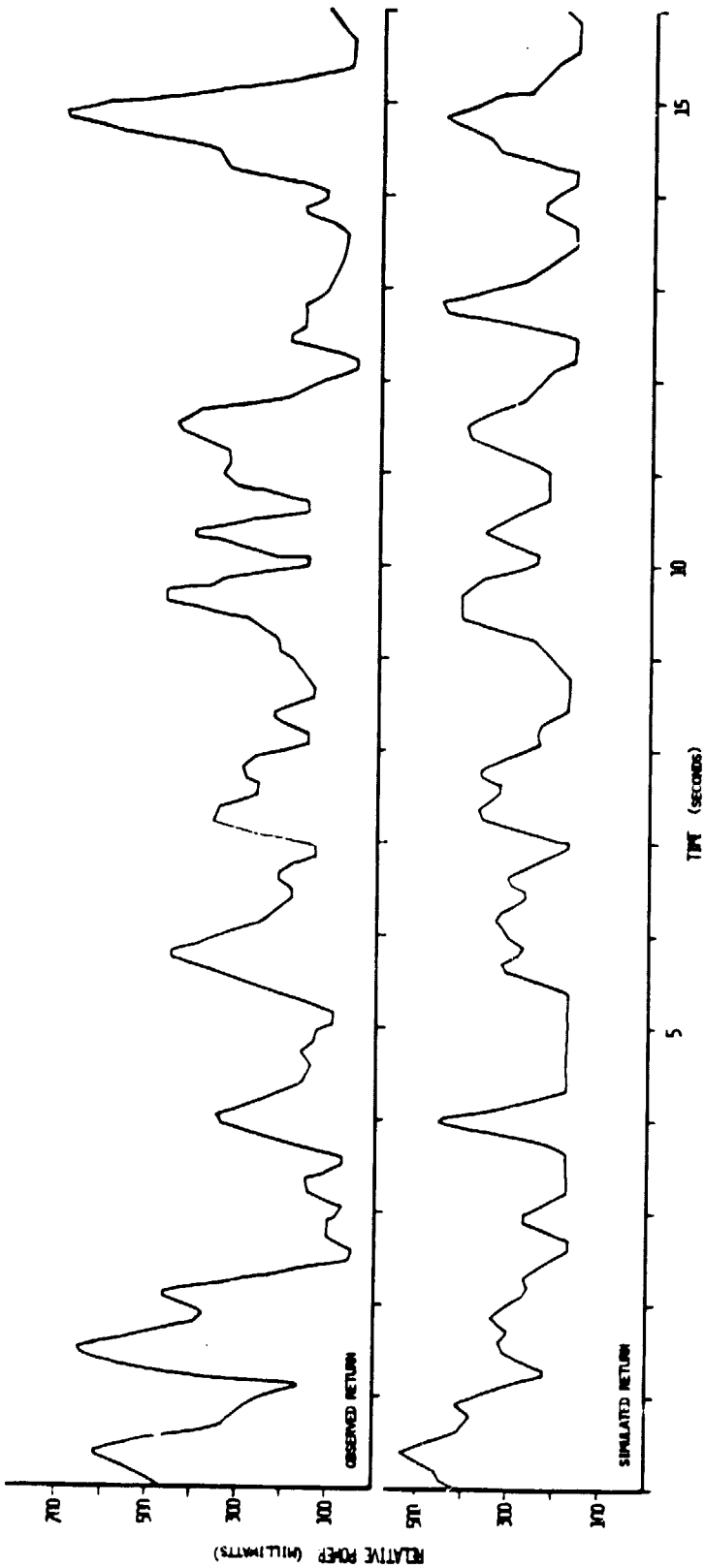

Figure 4.3. Plot of Initial Predicted Return and RADSCAT series

in ridged areas, and too large in areas of smooth ice. In addition, there is no variation in the simulated series in smooth areas.

An analysis of histograms of power versus ϕ, for both series, showed that the lack of resolution in smooth areas was caused by using only one bin for all flat ice. This produced an artificial grouping which effectively ignored the slope of the σ° curve. Increasing the number of bins by reducing the range width to 1° provided adequate resolution.

To adjust the simulated response for a better fit to the maxima and minima of the RADSCAT, it is necessary to consider the slope of the signature curves. Referring to Figure 3.1, note that the curve for flat ice is very non-linear, but over the narrow range 46-50° it can be approximated by a linear expression. Utilizing the slope-intercept form, the strength of return can be represented by

$$\sigma_f[\phi]_{dB} = m_f \cdot \phi + b_f \tag{4.2}$$

where m_f is the slope and b_f is the intercept. There is a similar approximation for $\sigma_r[\phi]_{dB}$.

With these approximations and Equations 3.7 and 4.1, p_{sim} can be calculated as

$$P_{sim} = \sum_{k} p(k)\ 10^{\left[(\sigma_r(\phi_k)_{dB}/10) + (\sigma_r(\phi_k)_{dB}/10)\right]}_{k = 1,2,\ldots,20} \tag{4.3}$$

where σ_r is, by definition, zero for flat ice, k = (9, 10, 11, 12), and σ_f is zero for all other k. The separation of σ_r and σ_f characteristics is reasonable since flat ice and rough ice are mutually exclusive.

To find the best fit of the two series in the training set, an iterative process was developed which adjusted m_f, m_r, b_f and b_r until the quantity

$$\sum_j [P_{sim}(j) - P_{R/S}(j)]^2 \qquad (4.4$$

was a minimum. That is, finding the least square error by adjusting these four variables produced the final model. Figure 4.4 shows plots of a portion of the training set time series along with the corresponding laser trace and photograms.

To evaluate the quality of the fit between the simulated and observed series, a statistical program developed by Service Data Corporation [25] was used on the NASA computer system, a CDC 6600. The correlation coefficient for the training set was .68. There were 716 data points, at 10 Hz, yielding 90% confidence bounds of 72% and 138%.

At this point, the "tuned" model was used on the independent evaluation set. All factors affecting the model remained the same. The only data manipulation on the evaluation set was that for feature alignment. The correlation coefficient for the evaluation set was .63, using 729 points at 10 Hz.

4.6 Stereo Analysis

Recall that the profile provided by the laser is effectively one-dimensional because of its narrow cell (.07 m), while the scatterometer has a resolution cell which is approximately 15 m wide.

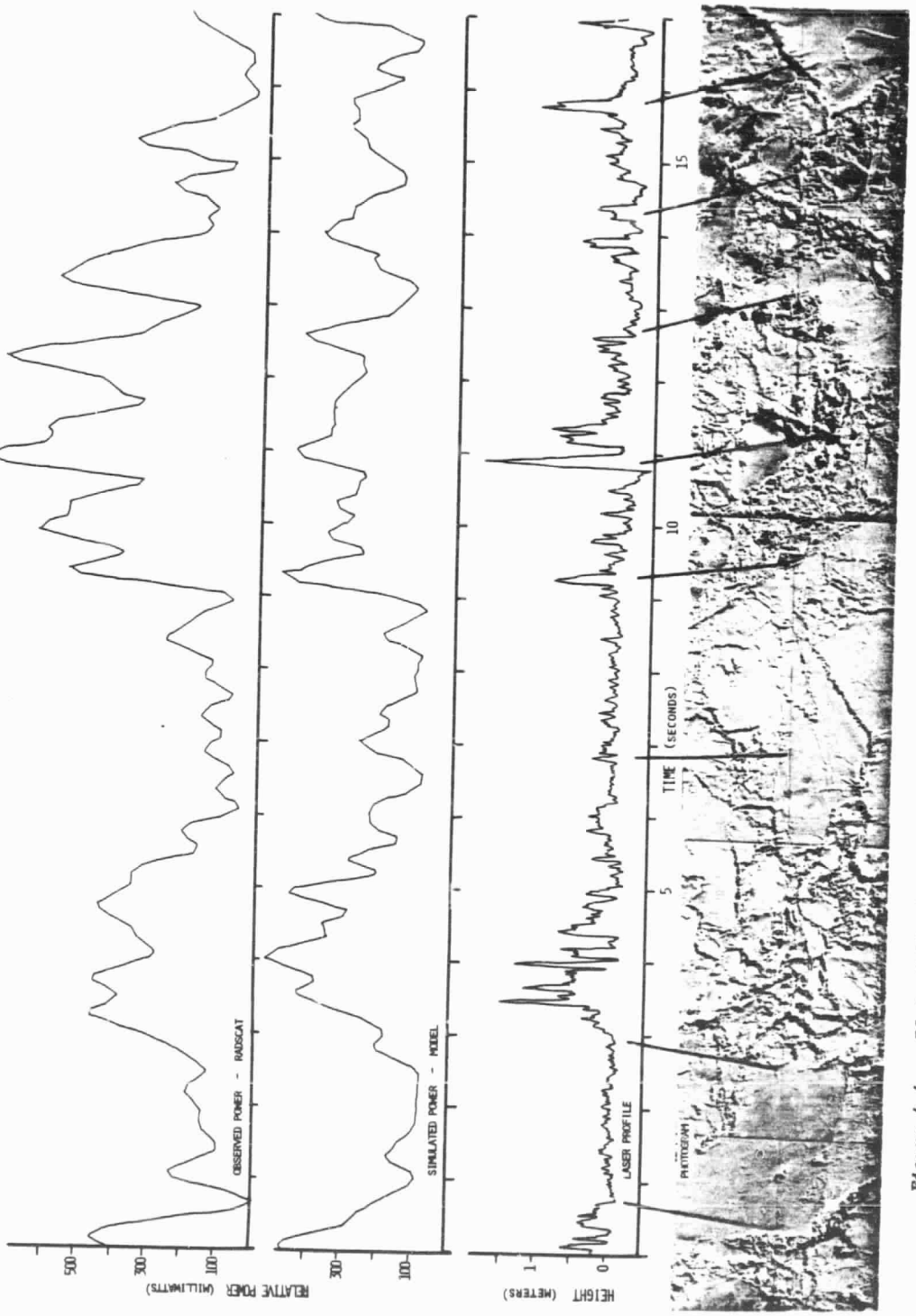

Figure 4.4. Plot of Final Predicted Return and RADSCAT series, with laser and photogram

The question which must be addressed is, can one laser profile somewhere within the footprint's width be truly representative of the average roughness seen by the scatterometer. To answer this, photographic stereo analysis was performed on two photograms to provide five parallel ice topography profiles within the antenna footprint. Figure 4.5 illustrates the location of the stereo profiles within the resolution cell.

One region (A) evaluated was a perpendicular crossing of isolated ridges composed of significantly high ridges with smooth ice to either side of them. The other region (B) was of significant roughness with one prominent ridge and little smooth ice. Figures 4.6 and 4.7 are facsimiles of the original photograms analyzed. Figures 4.8 and 4.9 are plots of the profiles along with the corresponding laser traces.

The stereo profiles for each region were pairwise correlated to determine their similarities. These correlation values are presented in Table 4.1, and are also shown plotted in Figure 4.10 as a function of the distance between the profiles. Note that the correlation drops to less than 50% within 28 feet, or approximately half the width of the RADSCAT footprint. To further describe the ice surface the mean and standard deviation of the heights were determined for each profile. These statistics are also presented in Table 4-1. Note the similarity of the statistics for the profiles in each area. Unfortunately, the laser profiles for these areas could not be correlated with the stereo profiles due to distortion introduced into

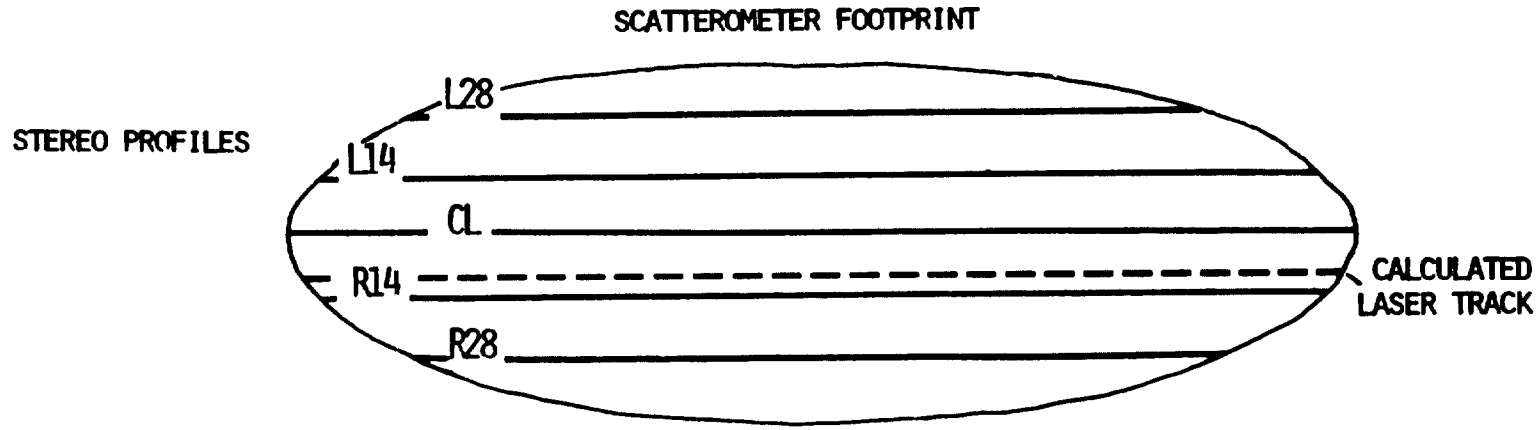

Figure 4.5. Illustration of Stereo Profiles Locations in the Resolution Cell

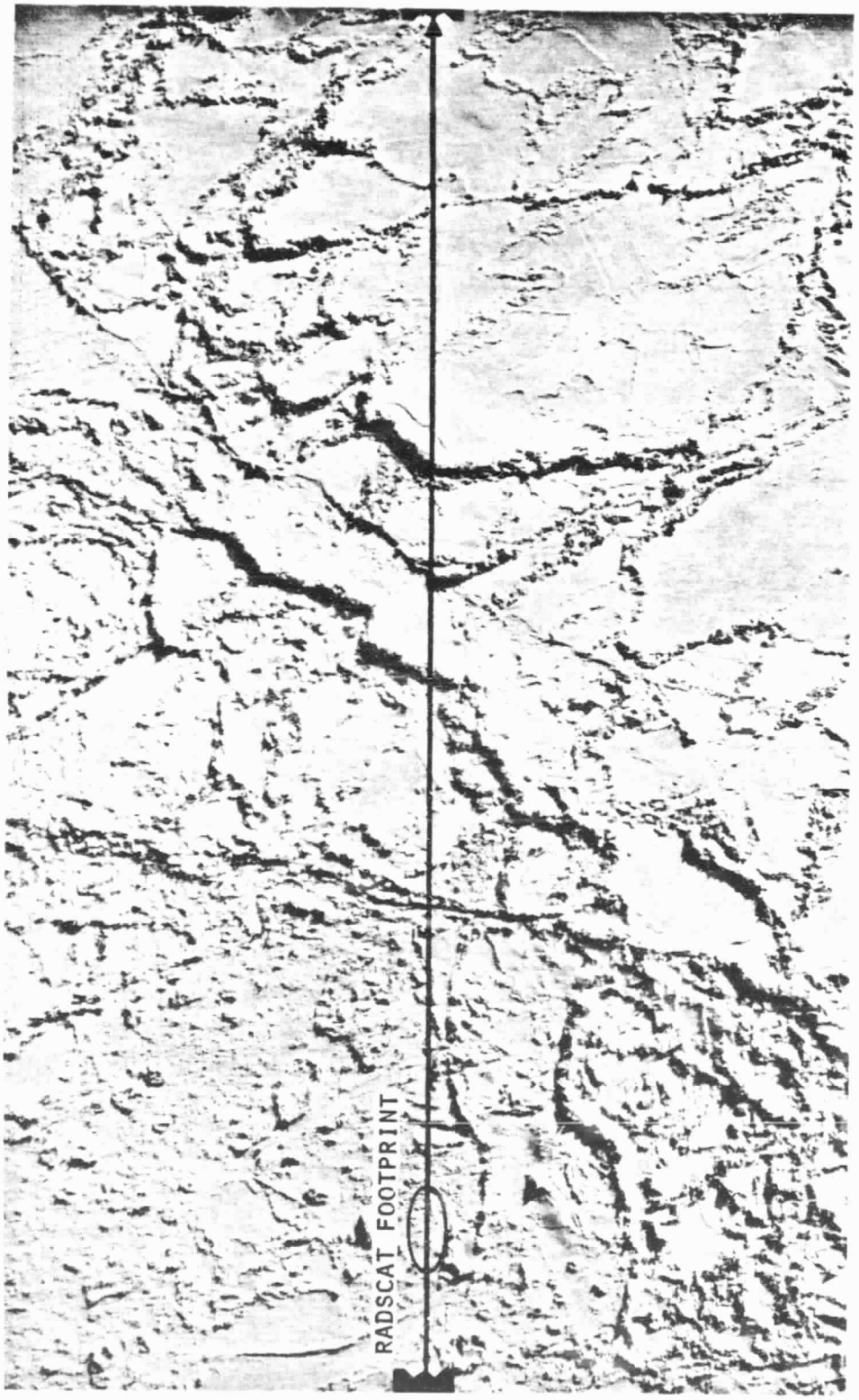

Figure 4.6. Facsimile of Aerial Photogram for Region A. Photo #05-370 NASA JSC 396, courtesy NASA Langley Research Center

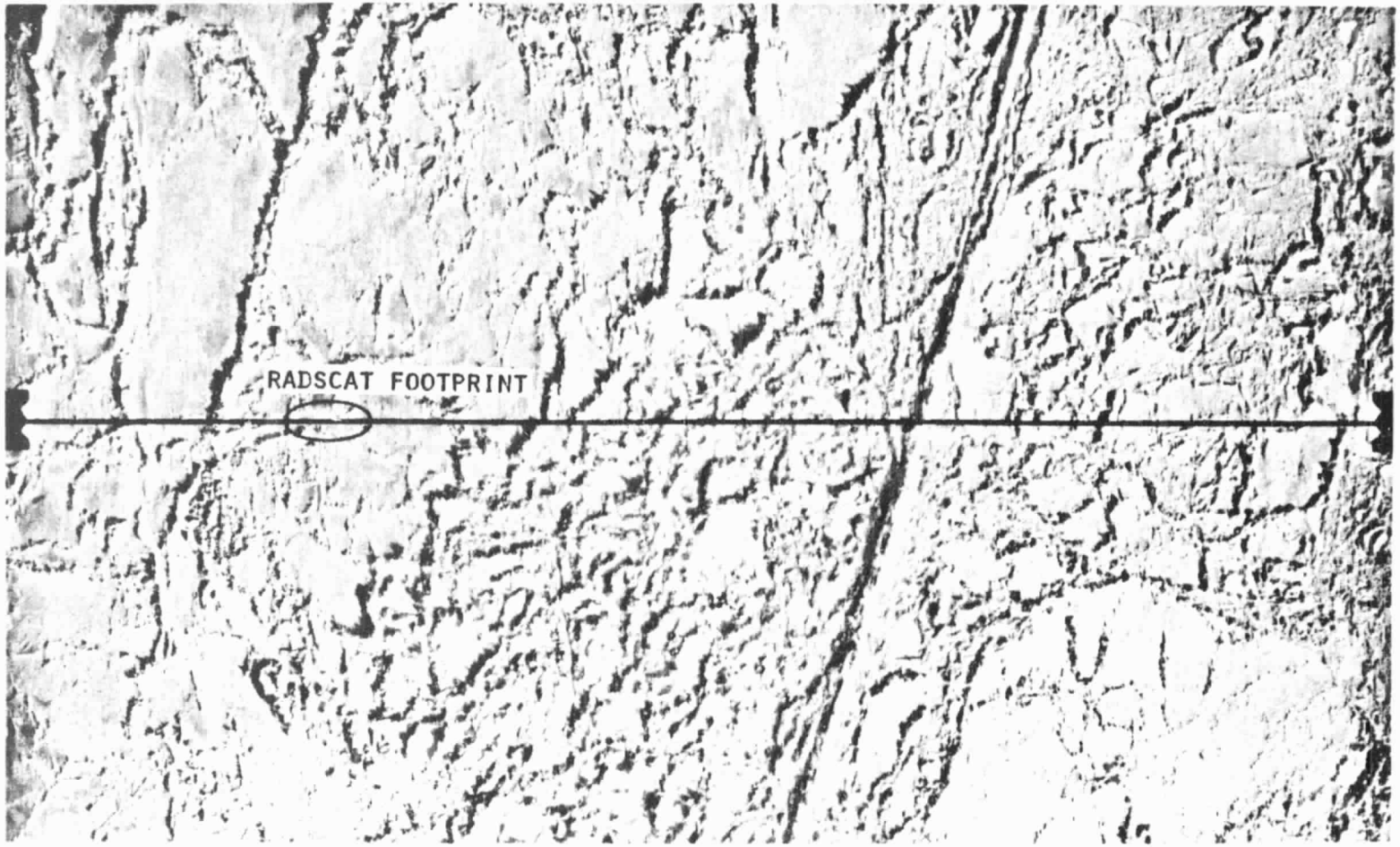

Figure 4.7. Facsimile of Aerial Photogram for Region B. Photo #05-405
NASA JSC 396, courtesy NASA Langley Research Center

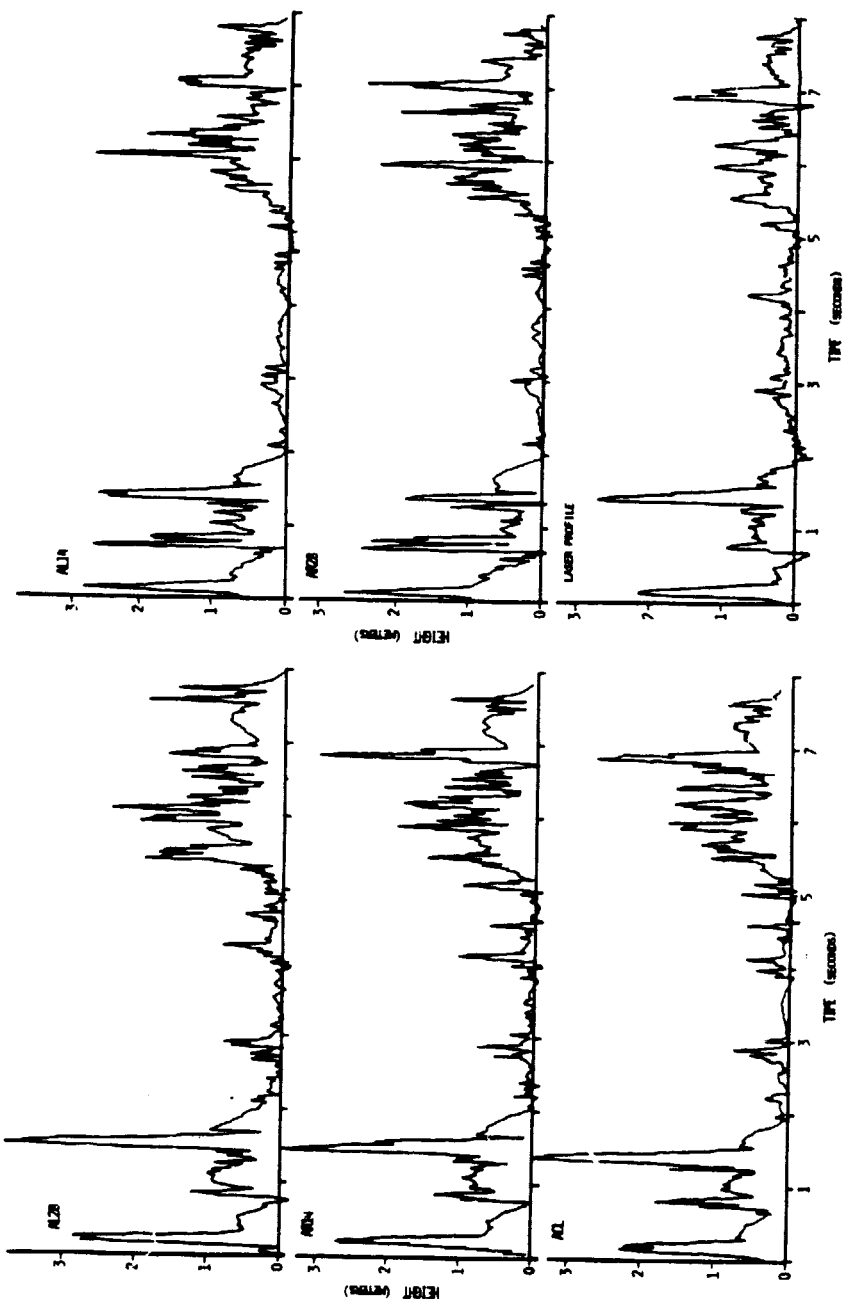

Figure 4.8. Stereo Profiles for Region A, with corresponding laser

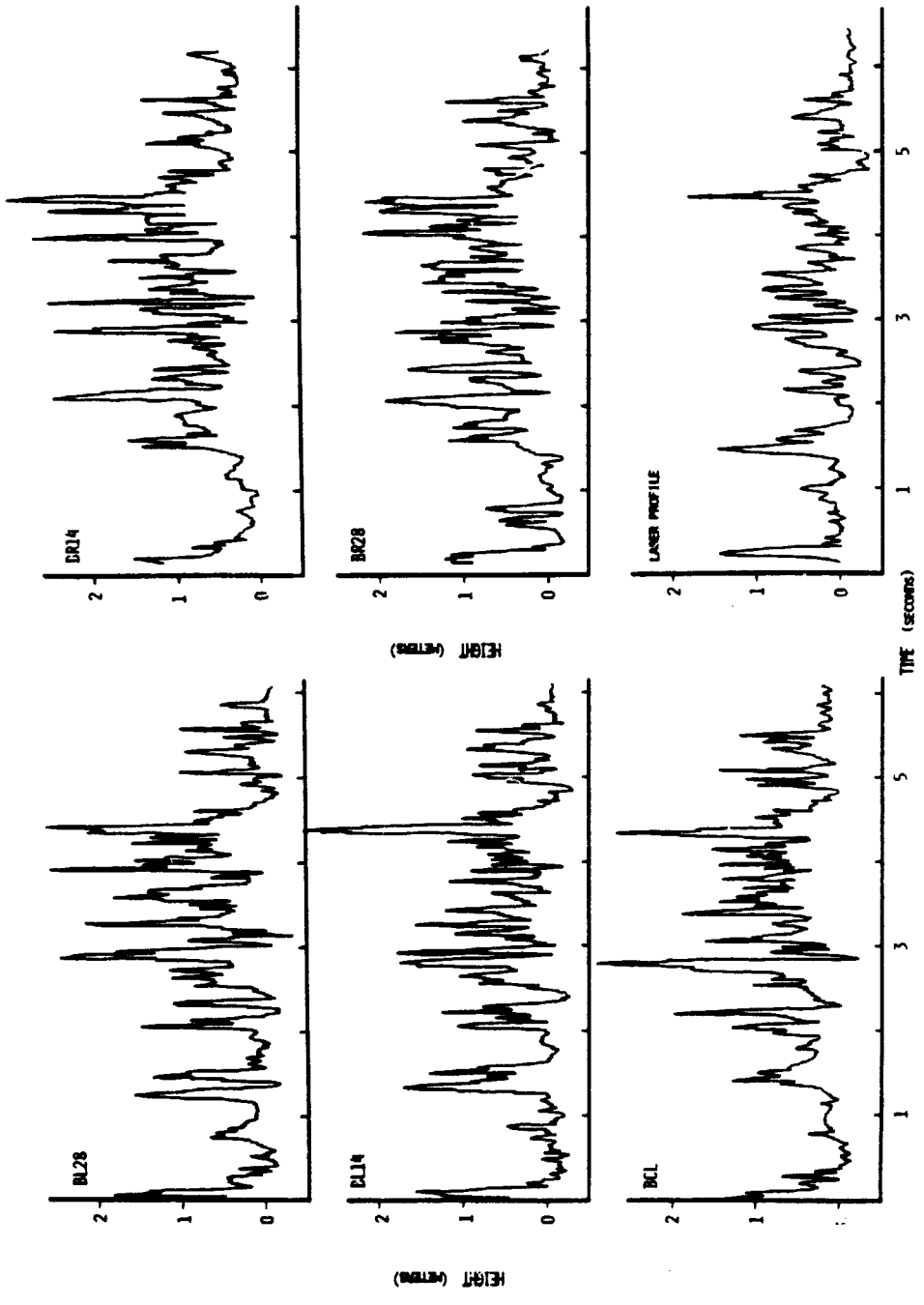

Figure 4.9. Stereo Profiles for Region B, with Corresponding laser

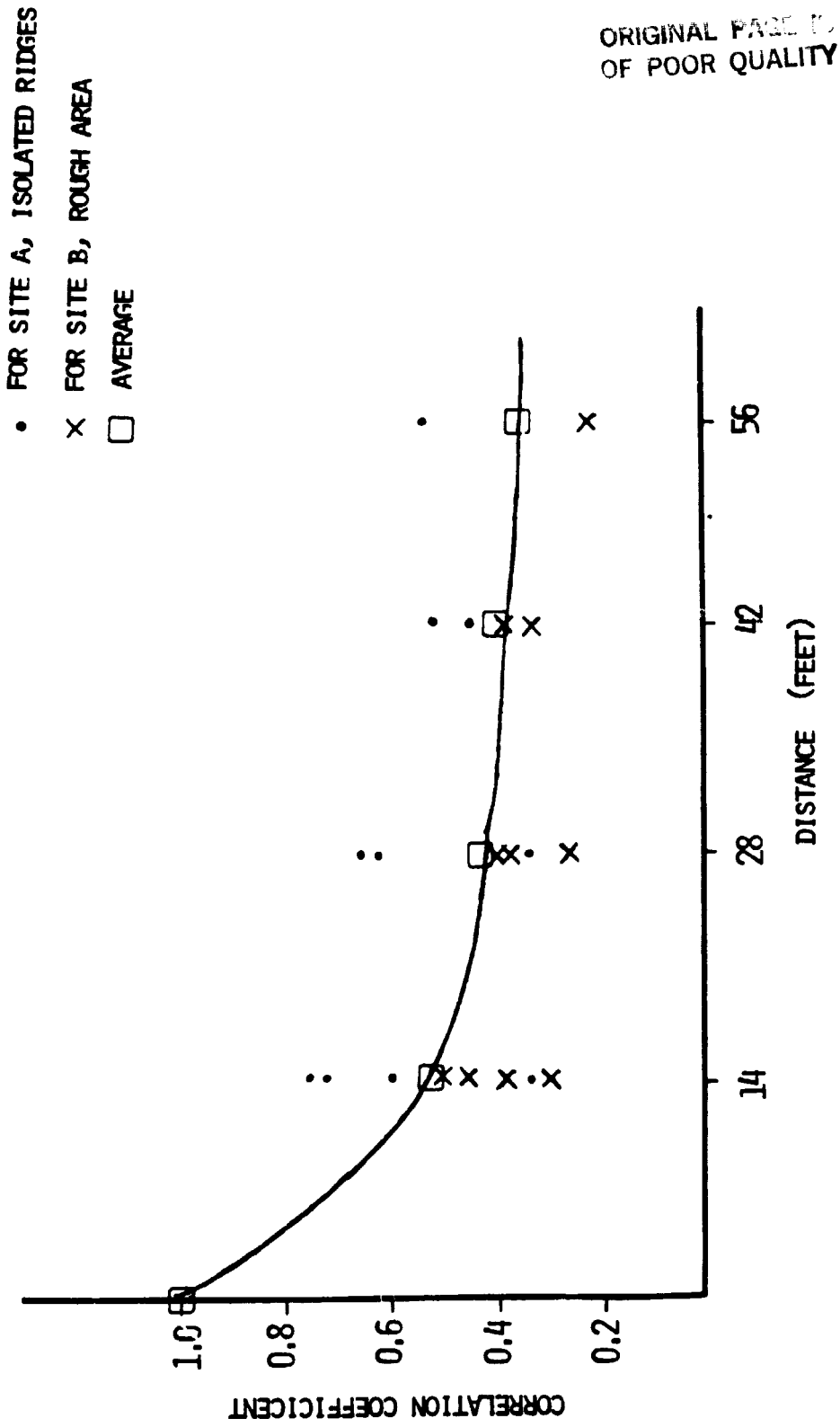

Figure 4.10. Plot of Decorrelation Time for Stereo Profiles

TABLE 4.1

REGION A	Statistics Mean	σ	rms	Cross Correlation xL28	xL14	xCL	xR14	xR28
28' left of center	4.30	.609	4.34	1.00	0.59	.61	0.44	0.56
14' left of center	4.26	.589	4.30		1.00	.72	.35	.52
center line	4.25	.615	4.29			1.00	.33	.66
14' right of center	4.18	.526	4.22				1.00	.70
28' right of center	4.19	.538	4.23					1.00
Δ max	.12	.089	.12					
REGION B								
28' left of center	3.58	.554	3.63	1.00	0.32	.27	.35	.22
14' left of center	3.55	.481	3.58		1.00	.53	.39	.25
center line	3.53	.490	3.57			1.00	.47	.36
14' right of center	3.58	.532	3.62				1.00	.38
28' right of center	3.62	.528	3.66					1.00
Δ max	.09	.073	.09					

the photography which caused a serious alignment problem between the two series. (Ice scientists currently addressing the question of the accuracy of the laser have been successful in aligning stereo-photograph profiles with the laser by using much longer time records [15].)

As a final evaluation, the stereo analysis profiles and their average were used as input to the model. The simulated returns due to each are shown as Figures 4.11 and 4.12, along with the $p_{R/S}$ for each area. Again, alignment problems due to distortion in the photography prevented us from correlating $p_{R/S}$ with these.

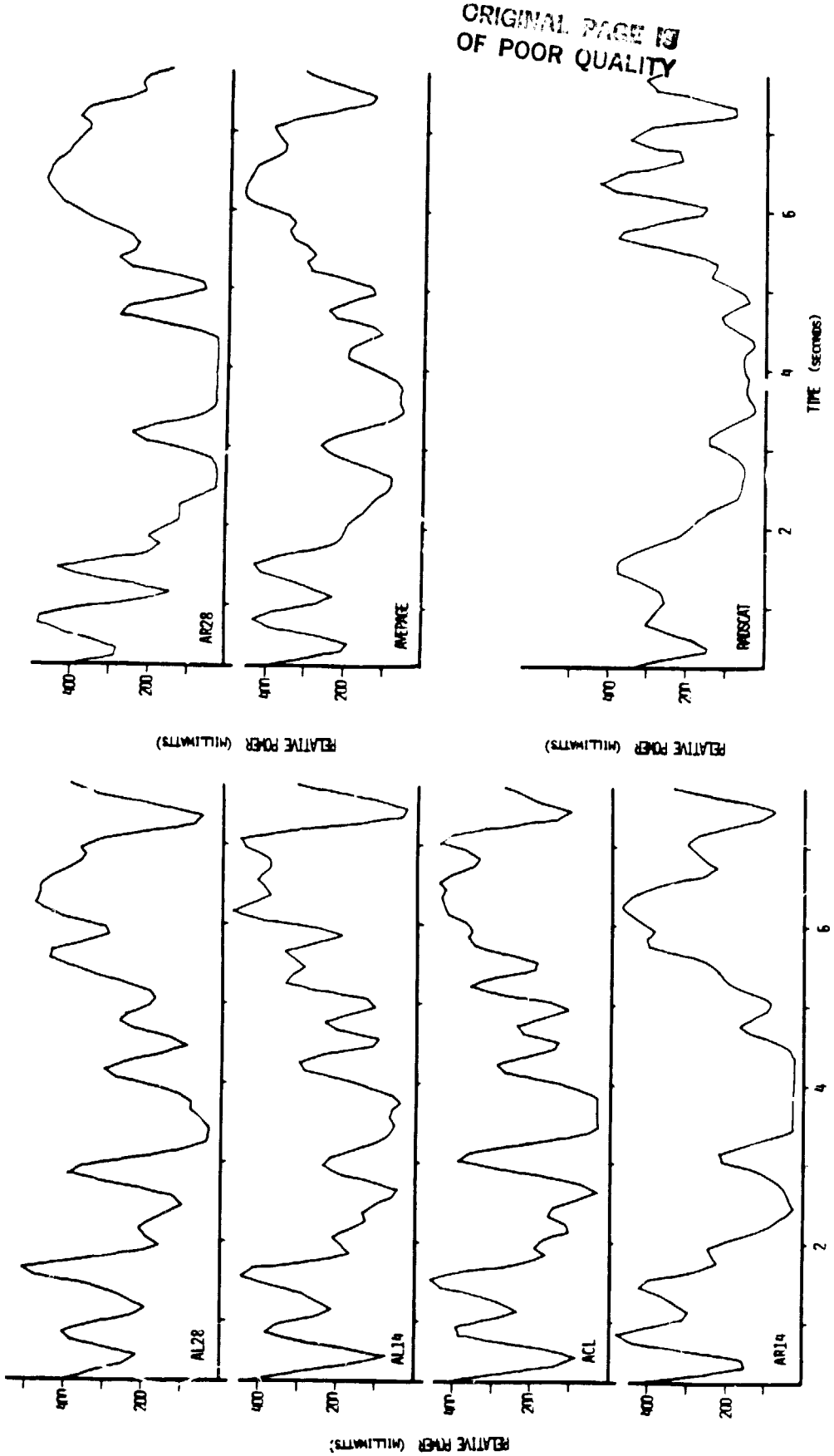

Figure 4.11. Plots of Predicted Return Based on Stereo Profiles for Region A

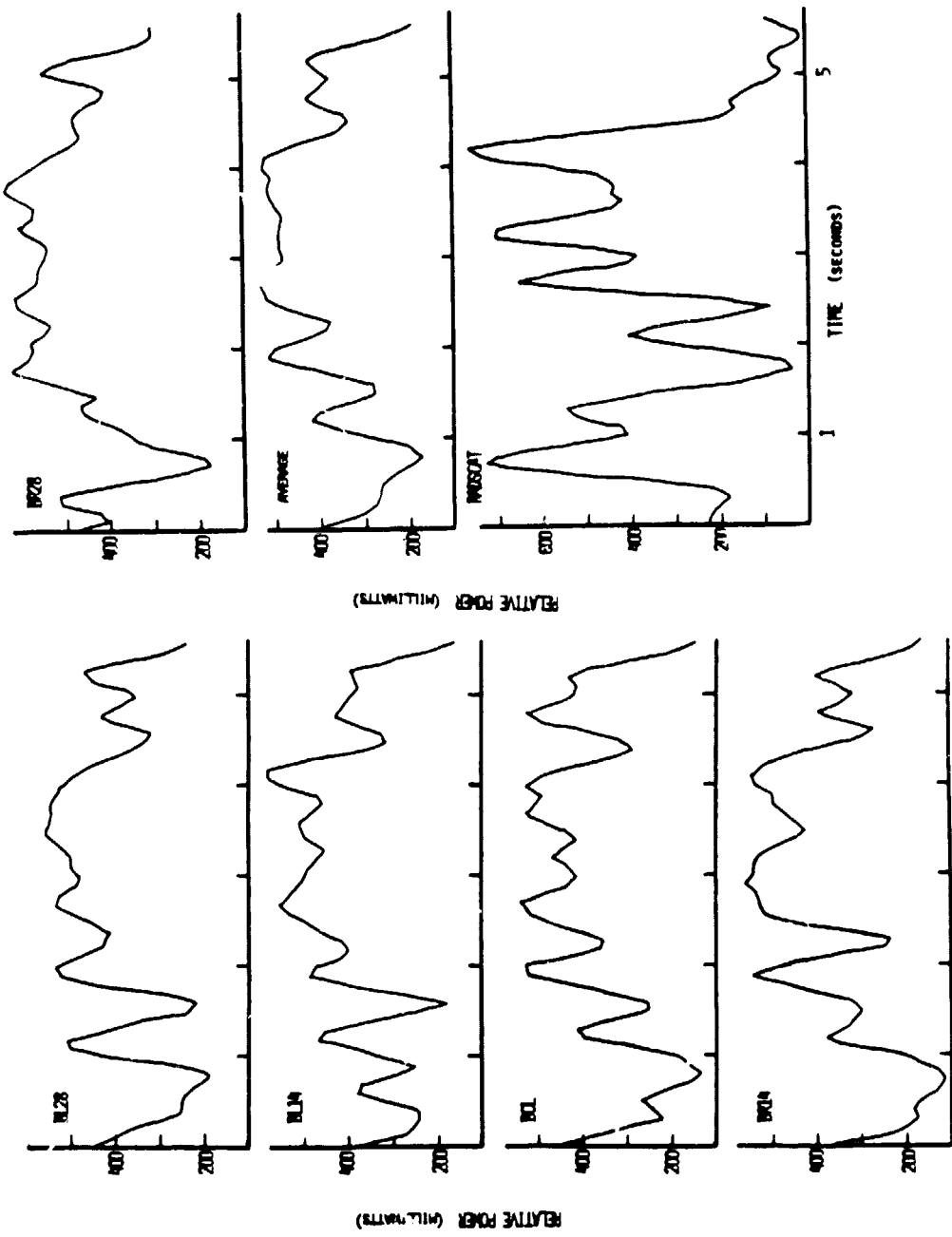

Figure 4.12. Plots of Predicted Return Based on Stereo Profiles for Region B

CHAPTER FIVE

CONCLUSIONS

5.1 Remarks

The goal of this thesis is to develop a model which uses one-dimensional surface topography to predict the backscattered power from ridged, first-year sea ice. Based on the empirical results presented in Chapter Four, we believe this goal has been achieved, within the limits of statistical uncertainty for geophysical data. As was stated in the introduction, we know of no work which has addressed the radar response to ice ridges. Existing backscatter models are theoretical in nature and are based on small scale (relative to wavelength) roughness. There are no established results with which to compare this model. It stands on its own merits as the first step in developing the algorithms necessary to interpret radar returns from ice.

The fact that the training set had a relatively high correlation coeffecient (.68) gives confidence that the model is well tuned. That the correlation is also relatively high (.62) for the evaluation set supports the conclusion that the model reasonably

simulates the response of the scatterometer. Further, since the input to the model is surface roughness it is reasonable to conclude that the scatterometer does respond to roughness and can be used in the future to indicate areas of ridging.

The results of the stereo analysis show that, while the statistics for the profiles of a homogeneous (as defined subjectively from photograms) area may be similar, their point-by-point comparison is not necessarily good. This is reasonable given the randomness which is inherent to ice roughness, particularly non-ridged rough areas such as area B in the analysis. The decrease in similarity in the profiles across widths comparable to the scatterometer footprint, as illustrated in Figure 4.11, indicate that a one-dimensional profile is not totally representative of the roughness within the footprint. Based on the correlation values though, it is an acceptable means of establishing the surface topography.

It is unfortunate that the stereo profiles could not be correlated with the laser or the RADSCAT series for the same areas, and thus provide statistical support for the model. However, the plots of these series shown in Chapter Four do show a visual agreement, particularly between the model output for the profile average across the footprint, which would indicate a reasonably tuned model.

5.2 Future Research

If research like that reported in this thesis is to continue it

will be necessary to find either a better way to determine the ice topography than a one-dimensional laser trace, or, since the use of stereo analysis has severe limitations, a way to verify that the one-dimensional trace can be used to establish the true topography across the width of the footprint, as well as along its length.

Another future research consideration is to develop the algorithms necessary to quantify the ice roughness given the radar response, since this is one of the needs of ice researchers. It will first be necessary to determine the parameter, or set of parameters, which can definitively describe the roughness of ice: something which may best be left to the physical scientists who have a more complete knowledge of the ice and its make-up. The microwave scientists can then develop a means of interpreting the backscatter in these terms.

Future research needs to consider also that sea ice, unfortunately, does not consist of discrete areas of first-year ice, homogeneous in roughness. For the large resolution cells necessary from satellite measurements, a means of interpreting the signature from areas of mixed ages and degrees of roughness must be established. Additionally, since, for the scatterometer, the response to multi-year ice is very similar to the response to roughness in first-year ice, it will be necessary to employ another sensor along with the scatterometer to provide accurate information about the ice age. At present, there is no way, without a priori knowledge of the surface, to differentiate between these two types of responses. Hopefully, the processing of the radar data to an absolute σ° will

provide the distinction needed. Until then, however, the passive radiometer would be a compatible choice since their responses complement each other.

REEFERENCES

[1] "NASA-Canada Carry out Arctic Ice Experiment", NASA Activities, Vol. 10. No. 5, May 1979

[2] W. F. Weeks, A. Kovacs and W. D. Hibler,III, "The Topography of Sea Ice", pending publication

[3] G. F. Herman and W. T. Johnson, "The Effect of Sea Ice Extent on the Climatology of the GISS General Circulation Model", presented at ICSI/Aidjex Symposium on Sea Ice Processes and Models, September 1977

[4] W. F. Weeks, "Overview - A Readers' Guide to the Seasonal Sea Ice Zone Workshop", Cold Regions Science and Technology, Vol. 2, 1980

[5] R. T. Gedney, W. L. Jones and H. R. Stanley, "Development of Active Microwave Remote Sensing Algorithms for Quantitative Measurement of Ice Properties with Emphasis on Ice Type and Surface Roughness Profile", Proposal, NASA Lewis, July 1978

[6] A. K. McQuillan and D.J. Clough, "Benefits of Remote Sensing Systems to Petroleum Operations in Canadian Ice Infested Waters", presented at Third Canadian Symposium on Remote Sensing, September, 1975

[7] E. Reimnitz and P. W. Barnes, "Sea Ice as a Geologic Agent on the Beaufort Sea Shelf of Alaska", The Coast and Shelf of the Beaufort Sea, December, 1974

[8] W. S. Dehn, "Ice Forecasting in the Beaufort Sea", The Coast and Shelf of the Beaufort Sea, December 1974

[9] W. F. Weeks, "The Potential of Remote Sensing", Oceanus. Vol. 24, No. 3, Fall, 1981

[10] S. J. Mock, A. D. Hartwell and W. D. Hibler III, "Spatial Aspects of Pressure Ridges", Aidjex Bulletin #12, February 1972

[11] W. D. Hibler, III, W. F. Weeks and S. J. Mock, "Statistical Aspects of Sea Ice Ridge Distributions", Aidjex Bulletin #12, February 1972

[12] S. K. Parashar, A. K. Fung and R. K. Moore, "A Theory of Wave Scatter from an Inhomogeneous Medium with a Slightly Rough Boundary and Its Application to Sea Ice", Remote Sensing of the Environment, No. 7, pp 37 to 50, 1978

[13] D. E. Barrick and W. H. Peake, "A Review of Scattering From Surfaces with Different Roughness Scales", Radio Science, Vol 3 No. 8, August 1968

[14] Operating Manual, Spectra Physics Geodolite 3A Laser Profiler, July 1969

[15] W. B. Tucker III, "A Note on the Accuracy of Laser Profiles of Sea Ice", Technical Note for Corps of Engineers, U. S. Army Cold Regions Research and Engineering Laboratory, December 1978

[16] J. W. Rouse, Jr., "Arctic Ice Type Identification by Radar", Proceedings of the I.E.E.E., Vol. 57, No. 4, April 1969

[17] J. W. Rouse, H. C. MacDonald and W. P. Waite, "Geoscience Application of Radar Sensors", I.E.E.E. Transactions on Geoscience Electronics, Vol. GE-7, No. 1, January 1969

[18] R. K. Moore, "Ground Echo", Radar Handbook, Chapter 25, 1970

[19] L. C. Schroeder, W. L. Jones and J. L. Mitchell, "Laboratory Calibration of AAFE RADSCAT". NASA TMX-73900, November 1976,

[20] S. K. Parashar, "Investigation of Radar Discrimination of Sea Ice", University of Kansas Center for Remote Sensing Technical Report 185-13, May 1974

[21] W. D. Hibler III, "Characterization of Cold Regions Terrain Using Airborne Laser Profilometry", Journal of Glaciology, Vol. 15, No. 73, 1975

[22] R. G. Onstott, "Near Surface Microwave Measurements of Arctic Sea Ice", presented at 2nd Workshop on the Microwave Remote Sensing of Sea Ice and Icebergs, April 1981

[23] A. E. Cross and W. L. Jones, Jr., "Measurements of AAFE RADSCAT Antenna Characteristics", NASA TMX-72844, June 1977

[24] F. B. Beck, "Antenna Pattern Corrections to Microwave Radiometer Temperature Calibrations", Radio Science, Vol. 10, No. 10, October, 1975

[25] D. Gridley, "A User's Guide to the Program for Time Series Analysis", NASA Contractor Report 165782, June, 1981

APPENDIX A

Referring to Figure A.1, the following are defined:

θ_n = Nadir Angle of the Antenna

B = 3dB Beamwidth of the Antenna, in radians

R = Slant Range = $\frac{\text{Altitude}}{\cos\theta_n}$

W = Width of the Footprint = 2 R tan(B/2)
= 2 R (B/2) (small angle approximation)
= R B

L = Length of Footprint (projection to normal) = $\frac{\text{Width}}{\cos\theta_n} = \frac{R\ B}{\cos\theta_n}$

A = Area of the Ellipse $= \frac{\pi(R\ B)(R\ B)}{4\cos\theta_n} = \frac{\pi R^2 B^2}{4\cos\theta_n}$

From the Radar Equation [18]

$$P_R = \frac{P_T G^2 \lambda^2 \sigma}{(4\pi)^3 R^4}$$

Where, P_R = received power
P_T = transmitted power
G = antenna gain
λ = wavelength
R = slant range
σ = radar cross section, the area intercepting that amount of power which, when scattered isotropically, produces an echo equal to that received from the object
σ° = the normalized radar cross section, or scattering coefficient,

For $\sigma^\circ = \frac{\sigma}{A}$ A, defined as above, is the area of the footprint

Then,

$$P_R = \frac{P_T G^2 \lambda^2 \sigma^\circ A}{(4\pi)^3 R^4} = \frac{P_T G^2 \lambda^2 \sigma^\circ R^2 B^2 \pi}{(4\pi)^3 R^4 4\cos\theta_n} = \frac{P_T G^2 \lambda^2 \sigma^\circ B^2}{256\pi^2 R^2 \cos\theta_n}$$

And,

$$\frac{P_R}{P_T} = \frac{G^2 \lambda^2 \sigma^\circ B^2}{256\pi^2 R^2 \cos\theta_n}$$

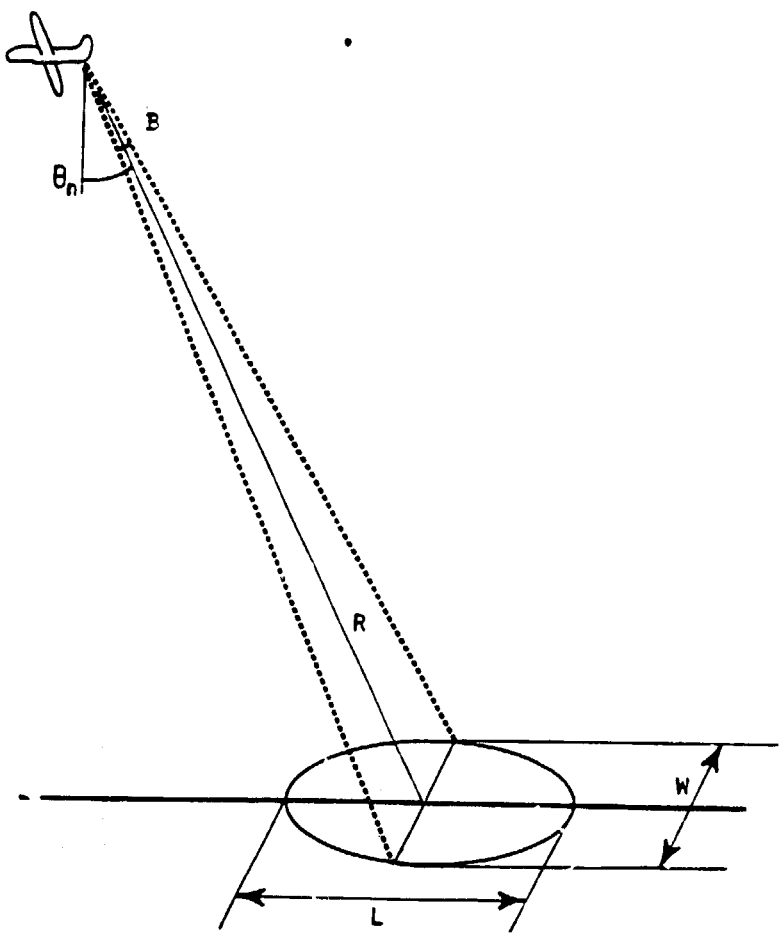

Figure A.1. Antenna Footprint on Surface

Referring to Figure A.2,

$$P_T = G_T P_X$$

For Calibrate, $v_{cal} = G_i P_{in} \alpha_i$ and $P_{in} = G_c P_X$

or, $v_{cal} = G_i G_c P_X \alpha_i$

(G_c is a loss, G_i is a gain, but is not long term stable)

Then,

$$v_{cal} = \frac{\alpha_i G_i G_c P_T}{G_T} \qquad (A.1)$$

For Operate, $v_{op} = G_i P_{in}$ and $P_{in} = G_R P_R$

Then,

$$v_{op} = G_i G_R P_R \qquad (A.2)$$

From A.1,

$$P_T = \frac{v_{cal} G_T}{\alpha_i G_i G_c}$$

From A.2,

$$P_R = \frac{v_{op}}{G_i G_R}$$

$$\frac{P_R}{P_T} = \frac{v_{op}}{G_i G_R} \cdot \frac{\alpha_i G_i G_c}{v_{cal} G_T} = \frac{\alpha_i v_{op} G_c}{v_{cal} G_R G_T}$$

From the Radar Equation,

$$\frac{P_R}{P_T} = \frac{G^2 \lambda^2 B^2 \sigma^\circ}{256 \pi^2 R^2 \cos\theta_n}$$

Solving for σ°,

$$\sigma^\circ = \frac{256 \pi^2 \alpha_i v_{op} G_c R^2 \cos\theta_n}{v_{cal} G_R G_T G^2 \lambda^2 B^2}$$

Note that G_i has been eliminated

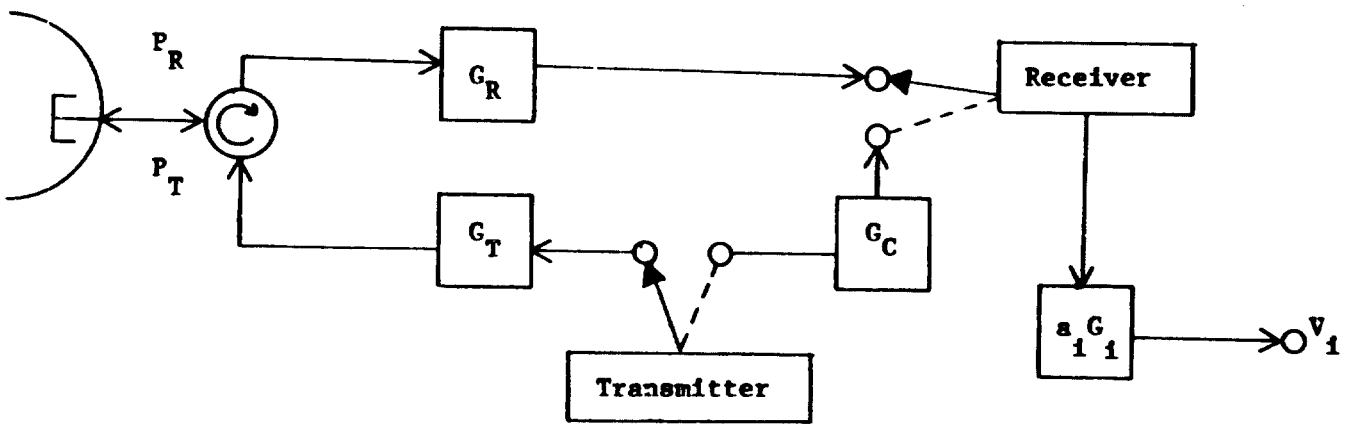

during Calibrate: receiver is on while transmitter is on
during Operate: receiver is off while transmitter is on

Figure A.2. RADSCAT Flowchart